Correlated isotopic and chemical evidence for condensation origins of olivine in comet 81P/Wild 2 and in AOAs from CV and CO chondrites

Kohei Fukuda [a,*], Donald E. Brownlee [b], David J. Joswiak [b], Travis J. Tenner [c], Makoto Kimura [d], Noriko T. Kita [a]

[a] WiscSIMS, Department of Geoscience, University of Wisconsin-Madison, Madison, WI 53706, USA
[b] Department of Astronomy, University of Washington, Seattle, WA 98195, USA
[c] Chemistry Division, Nuclear and Radiochemistry, Los Alamos National Laboratory, MSJ514, Los Alamos, NM 87545, USA
[d] National Institute of Polar Research, Tokyo 190-8518, Japan

Abstract

Magnesium stable isotope ratios and minor element abundances of five olivine particles from comet 81P/Wild 2 were examined by secondary ion mass spectrometry (SIMS). Wild 2 olivine particles exhibit only small variations in δ^{25}Mg values from $-1.0\ ^{+0.4}/_{-0.5}$‰ to $0.6\ ^{+0.5}/_{-0.6}$‰ (2σ). This variation can be simply explained by mass-dependent fractionation from Mg isotopic compositions of the Earth and bulk meteorites, suggesting that Wild 2 olivine particles formed in the chondritic reservoir with respect to Mg isotope compositions. We also determined minor element abundances, and O and Mg isotope ratios of olivine grains in amoeboid olivine aggregates (AOAs) from Kaba (CV3.1) and DOM 08006 (CO3.01) carbonaceous chondrites. Our new SIMS minor element data reveal uniform, low FeO contents of $\sim$0.05 wt% among AOA olivines from DOM 08006, suggesting that AOAs formed at more reducing environments in the solar nebula than previously thought. Furthermore, the SIMS-derived FeO contents of the AOA olivines are consistently lower than those obtained by electron microprobe analyses ($\sim$1 wt% FeO), indicating possible fluorescence from surrounding matrix materials and/or Fe,Ni-metals in AOAs during electron microprobe analyses. For Mg isotopes, AOA olivines show more negative mass-dependent fractionation (-3.8 ± 0.5‰ $\leq \delta^{25}$Mg $\leq -0.2 \pm 0.3$‰; 2σ) relative to Wild 2 olivines. Further, these Mg isotope variations are correlated with their host AOA textures. Large negative Mg isotope fractionations in olivine are often observed in pore-rich AOAs, while those in compact AOAs tend to have near-chondritic Mg isotopic compositions. These observations indicate that pore-rich AOAs preserved their gas–solid condensation histories, while compact AOAs experienced thermal processing in the solar nebula after their condensation and aggregation. Importantly, one ^{16}O-rich Wild 2 LIME olivine particle (T77/F50) shows negative Mg isotope fractionation (δ^{25}Mg $= -0.8 \pm 0.4$‰, δ^{26}Mg $= -1.4 \pm 0.9$‰; 2σ) relative to bulk chondrites. Minor element abundances of T77/F50 are in excellent agreement with those of olivines from pore-rich AOAs in DOM 08006. The observed similarity in O and Mg isotopes, and minor element abundances suggest that T77/F50 formed in an environment similar to AOAs, probably near the proto-Sun, and then was transported to the Kuiper belt, where comet 81P/Wild 2 likely accreted.
© 2020 Elsevier Ltd. All rights reserved.

Keywords: Magnesium three-isotopes; Comet 81P/Wild 2; Amoeboid olivine aggregates; Early Solar System; Secondary ion mass spectrometry

* Corresponding author.
    E-mail address: kfukuda2@wisc.edu (K. Fukuda).

1. INTRODUCTION

Particles collected from the Jupiter family comet 81P/Wild 2 (NASA Stardust mission) have provided unique opportunities to study materials from the outer Solar System, likely within the Kuiper Belt (Brownlee et al., 2006, 2012; Brownlee, 2014). Wild 2 particles consist of a variety of materials, including presolar grains (McKeegan et al., 2006; Messenger et al., 2009; Leitner et al., 2010, 2012) and organic matter (Sandford et al., 2006; Sandford, 2008; Matrajt et al., 2008) as well as numerous high temperature materials such as Ca, Al-rich inclusions (CAIs; e.g., McKeegan et al., 2006; Zolensky et al., 2006; Chi et al., 2009; Simon et al., 2008; Joswiak et al., 2012, 2017) and ferromagnesian silicates (Nakamura et al., 2008; Bridges et al., 2012; Joswiak et al., 2012; Nakashima et al., 2012; Ogliore et al., 2012; Frank et al., 2014; Gainsforth et al., 2015; Defouilloy et al., 2017). Determining the origins of such particles can shed light on dynamic properties of the solar protoplanetary disk, including transport and processing of comet precursors. For example, the existence of high temperature minerals in Wild 2 suggests that materials originating from the hotter inner part of the solar protoplanetary disk were transported outward to the cooler Kuiper Belt region and eventually accreted to comets (e.g., McKeegan et al., 2006; Ciesla, 2007; Nakamura et al., 2008; Brownlee et al., 2012). In addition, Nakashima et al. (2012) suggested that at least a fraction of the ferromagnesian silicates in comet Wild 2 formed in the outer regions of the asteroid belt, based on the observed similarity of oxygen isotope systematics between Wild 2 particles and chondrules from CR chondrites. Furthermore, Bridges et al. (2012) hypothesize an outer Solar System origin for some Wild 2 silicate particles that have similar oxygen isotope and elemental characteristics when compared to Al-rich chondrules from carbonaceous chondrites. Therefore, at least some Wild 2 silicate particles may also hold information about the physicochemical conditions of the outer Solar System where comets accreted.

In the past decade, oxygen three-isotope ratios of forty-seven Wild 2 silicate particles larger than 2 μm have been acquired by secondary ion mass spectrometry (SIMS) (McKeegan et al., 2006; Nakamura et al., 2008; Nakamura-Messenger et al., 2011; Bridges et al., 2012; Nakashima et al., 2012; Ogliore et al., 2012, 2015; Joswiak et al., 2014; Gainsforth et al., 2015; Defouilloy et al., 2017; Chaumard et al., 2018), and they show a bimodal distribution on an oxygen three-isotope diagram (Fig. 1). The mass-independent fractionation of oxygen isotopes among Wild 2 particles are expressed as $\Delta^{17}O$ ($=\delta^{17}O - 0.52 \times \delta^{18}O$, where $\delta^{17,18}O = [(^{17,18}O/^{16}O)_{sample}/(^{17,18}O/^{16}O)_{VSMOW} - 1] \times 1000$; VSMOW = Vienna Standard Mean Ocean Water; Baertschi, 1976), and range from –24‰ to +3‰ for all data with uncertainties smaller than 5‰. Among them, the $\Delta^{17}O$ values of thirty-six Wild 2 particles ($\geq$2 μm) range from –7‰ to +3‰ (McKeegan et al., 2006; Nakamura et al., 2008; Nakashima et al., 2012; Ogliore et al., 2012, 2015; Joswiak et al., 2014; Gainsforth et al., 2015; Defouilloy et al., 2017; Chaumard et al., 2018), similar to those of chondrules found in chondrites
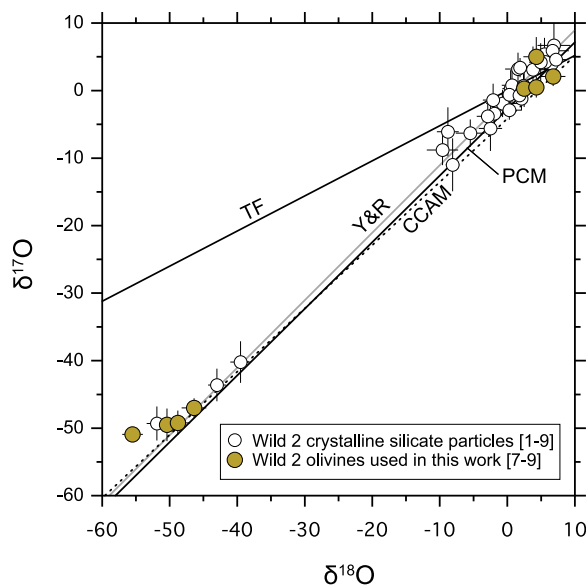

Fig. 1. Oxygen three-isotope ratios of Wild 2 crystalline silicate particles larger than 2 μm with uncertainties of $\Delta^{17}O$ smaller than 5‰. TF, Y&R, CCAM, and PCM represent terrestrial fractionation (Clayton et al., 1991), the Young and Russell (Young and Russell, 1998), the carbonaceous chondrite anhydrous mineral (Clayton et al., 1977), and primitive chondrule mineral (Ushikubo et al., 2012, 2017) lines, respectively. Average values for each particle are shown. Data from [1] McKeegan et al. (2006), [2] Nakamura et al. (2008), [3] Ogliore et al. (2012, 2015), [4] Bridges et al. (2012), [5] Joswiak et al. (2014), [6] Gainsforth et al. (2015), [7] Nakashima et al. (2012), [8] Defouilloy et al. (2017), [9] Chaumard et al. (2018). Two particles, Torajiro and Gozen-sama, that show heterogeneous O isotope ratios within a single particle (Nakamura et al., 2008) are not shown.

(Tenner et al., 2018a). In contrast, seven Wild 2 particles show more ^{16}O-rich oxygen isotopic characteristics ($\Delta^{17}O = $ –24‰ to –20‰). These seven particles are nearly pure forsterite or enstatite, some of which are low-iron, manganese-enriched (LIME) olivines and pyroxenes (Nakashima et al., 2012; Defouilloy et al., 2017; Chaumard et al., 2018). LIME olivines and pyroxenes (hereafter LIME silicates) have MnO/FeO (wt%) ratios much higher than 0.1 and low FeO contents (typically $\leq$1 wt%). As Mn is not stable as metal at solar nebula conditions, it likely condensed at ~1100 K, as Mn_2SiO_4 in solid solution with forsterite, and as $MnSiO_3$ with enstatite (Larimer, 1967; Wai and Wasson, 1977; Lodders, 2003). In contrast, Fe co-condenses as metal with forsterite (if the oxidation state is below the Fe-FeO buffer), meaning that high MnO/FeO ratios observed in LIME silicates suggest a condensation origin from the solar nebula (Klöck et al., 1989; Weisberg et al., 1993, 2004; Ebel et al., 2012). LIME silicates have been found in chondritic interplanetary dust particles (IDPs) (Klöck et al., 1989) that are believed to have a cometary origin (e.g., Bradley, 2003 and references therein), implying that LIME silicates may have been abundant nebular condensates and they were present in comet accretion regions. Thus, Wild 2 LIME silicates contain important clues for understanding the formation and transportation of solids in the early Solar System.

LIME silicates are also observed in amoeboid olivine aggregates (AOAs; e.g., Weisberg et al., 2004; Komatsu et al., 2015) that are the most common type of refractory inclusions in carbonaceous chondrites (e.g., Krot et al., 2004a and references therein; Sugiura et al., 2009; Ruzicka et al., 2012; Krot et al., 2014). Based on their irregularly-shaped, porous, and fine-grained textures, AOAs are thought to be aggregates of solids condensed from the solar nebula and appear to have avoided significant melting after aggregation (e.g., Grossman and Steele, 1976; Komatsu et al., 2001, 2009; Krot et al., 2004a and references therein; Weisberg et al., 2004; Sugiura et al., 2009; Han and Brearley, 2015). In addition, Mg stable isotope ratios of AOAs are indicative of a condensation origin. δ^{25}Mg values of bulk AOAs (where δ^{25}Mg = $[(^{25}Mg/^{24}Mg)_{sample}/(^{25}Mg/^{24}Mg)_{DSM-3} - 1] \times 1000$; per-mil deviation from Mg reference material DSM-3; Galy et al., 2003) range from –2.47‰ to –0.03‰ (Larsen et al., 2011; Olsen et al., 2011), some of which are negatively fractionated from those of bulk chondrites (δ^{25}Mg = –0.15 ± 0.04‰; Teng et al., 2010). In situ SIMS Mg isotope analyses of AOA olivines also show similar variations in δ^{25}Mg values, as low as ~–2.8‰ (MacPherson et al., 2012; Ushikubo et al., 2017; Marrocchi et al., 2019a). The light isotope enrichments observed in AOAs may be the result of disequilibrium condensation from solar nebula gas due to kinetic isotope fractionation (Richter, 2004). Note that AOAs from the least metamorphosed chondrites are ^{16}O-rich (Δ^{17}O < –20‰; Aléon et al., 2002; Fagan et al., 2004; Krot et al., 2004a; Itoh et al., 2007; Yurimoto et al., 2008 and references therein; Ushikubo et al., 2017; Komatsu et al., 2018). The similarities in oxygen isotope ratios and mineral chemistry (i.e., ^{16}O-rich oxygen isotope signatures and the occurrence of LIME silicates) suggest a genetic link between Wild 2 LIME silicates and AOAs (Nakashima et al., 2012; Defouilloy et al., 2017). However, unlike AOAs, the petrological context of ^{16}O-rich Wild 2 particles is not well understood because most particles have been found as single mineral grains. If these particles formed by disequilibrium condensation, their Mg isotope ratios could be enriched in lighter isotopes (Richter, 2004), which could be used to trace condensation processes. Due to small particle sizes (<10 μm), Mg isotope data from Wild 2 particles at sub-‰ precision are currently lacking, but would nonetheless be valuable for testing condensation hypotheses for ^{16}O-rich Wild 2 particles.

Here, we report Mg three-isotope ratios and minor element concentrations of eight Wild 2 olivine particles (four that are ^{16}O-rich and four that are ^{16}O-depleted) in order to better understand their formation processes. To obtain high spatial resolution (≤2 μm) SIMS Mg isotope analyses, we upgraded the WiscSIMS Cameca IMS 1280 with a radio frequency (RF) plasma oxygen ion source (Hertwig et al., 2019) and applied an instrumental bias correction method that combines forsterite endmember values (=Mg/[Mg + Fe] molar %) and secondary ion Mg^+/Si^+ ratios (Fukuda et al., 2020). We also conducted SIMS O and Mg isotope analyses, and SIMS minor element analyses of olivine grains in AOAs from Kaba (CV3.1; Bonal et al., 2006) and the least metamorphosed CO chondrite

DOM 08006 (classified as CO3.00 from Davidson et al., 2019, while we adopt CO3.01 from Fe,Ni-metal analyses of Tenner et al., 2018b), in order to compare their formation histories with those of Wild 2 particles.

2. WILD 2 SAMPLES

Eight Wild 2 olivine particles were analyzed from four Stardust tracks (Track 57, 77, 149, and 175) including one particle from track 57 (T57/F10), four particles from track 77 (T77/F4, T77/F6, T77/F7, and T77/F50), two particles from track 149 (T149/F1 and T149/F11a), and one particle from track 175 (T175/F1). Secondary electron images of the eight Wild 2 olivine particles are shown in Fig. 2. Mineral chemistry and oxygen isotope ratios of these particles have been previously reported (Joswiak et al., 2012; Nakashima et al., 2012; Defouilloy et al., 2017; Chaumard et al., 2018). Oxygen isotope ratios of the eight Wild 2 particles (Nakashima et al., 2012; Defouilloy et al., 2017; Chaumard et al., 2018) are shown in Fig. 1. Four of eight particles are ^{16}O-rich (T57/F10, T77/F6, T77/F50, and T175/F1) while the other four particles are ^{16}O-depleted (T77/F4, T77/F7, T149/F1, and T149/F11a). Fo contents (Fo = Mg/[Mg + Fe] molar %) of the ^{16}O-rich particles range from 98.0 to 99.8, while ^{16}O-depleted particles are more FeO-rich (Fo$_{60–85}$) (Joswiak et al., 2012; Defouilloy et al., 2017; Chaumard et al., 2018). Among the ^{16}O-rich particles, T77/F6 and T77/F50 were found in the same bulbous track identified as T77 (type B track; Hölz et al., 2006; Burchell et al., 2008; Joswiak et al., 2012). It was suggested that the original projectile was a loose aggregate and that the two ^{16}O-rich particles as well as the other ^{16}O-rich particle in the same track (T77/F104) which are co-linearly aligned were derived from a single grain that fragmented during capture (Joswiak et al., 2012).

3. ANALYTICAL PROCEDURES

3.1. Electron microscopy

Two thin sections, Kaba USNM 1052-1 and DOM 08006, 50, were allocated from the Smithsonian Institution and NASA JSC, respectively. Backscattered electron (BSE) and secondary electron (SE) images of individual AOAs were obtained with a Hitachi S-3400 scanning electron microscope (SEM) at the University of Wisconsin-Madison (UW-Madison). Major and minor elements (Na$_2$O, MgO, Al$_2$O$_3$, SiO$_2$, K$_2$O, CaO, TiO$_2$, Cr$_2$O$_3$, MnO, and FeO) of minerals in AOAs were obtained with a Cameca SXFive FE electron-probe microanalyzer (EPMA) at UW-Madison. EPMA analyses were performed with an accelerating voltage of 15 kV and a beam current of 20 nA, with a 3 micron diameter beam. Off peak backgrounds were acquired, with 10 second counts on the background and 10 seconds on the peaks. The following reference materials (RMs) were used for olivine analyses: Burma jadeite (Na), synthetic forsterite (Mg, Si), Grass Valley anorthite (Al), NMNH 122142 Kakanui augite (Ca), microcline (K), TiO$_2$ oxide (Ti), synthetic Cr$_2$O$_3$ (Cr), synthetic Mn$_2$SiO$_4$ (Mn), and synthetic FeO (Fe). For high-Ca
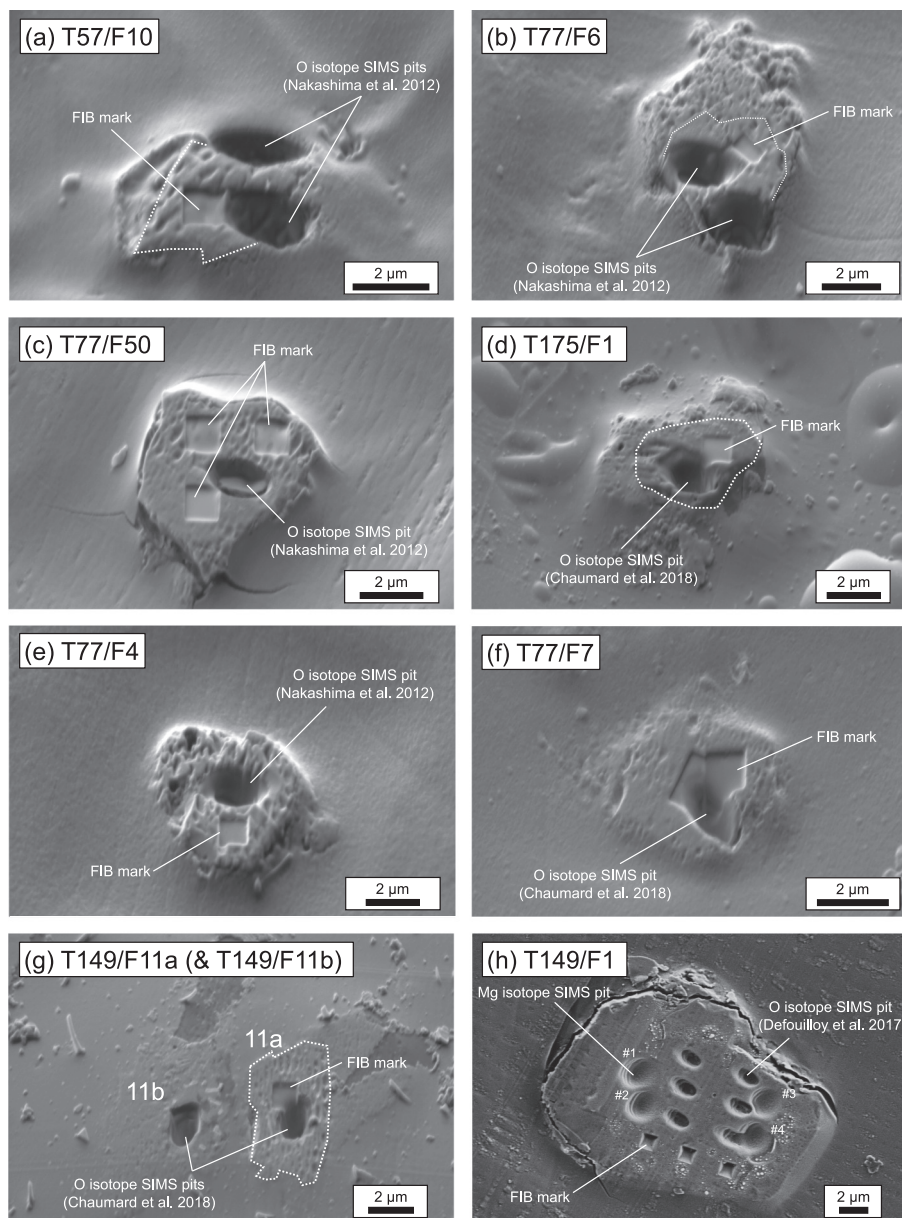
Fig. 2. SE images of the eight comet 81P/Wild 2 olivine particles before (a-g) and after (h) SIMS Mg isotope analyses. (a–d) ^{16}O-rich olivine particles (a) T57/F10, (b) T77/F6, (c) T77/F50, (d) T175/F1. (e–h) ^{16}O-depleted olivine particles (e) T77/F4, (f) T77/F7, (g) T149/F11a (and T149/F11b; not used in this study), (h) T149/F1. For all images, SIMS pits of previous oxygen isotope analyses are visible (Nakashima et al., 2012; Defouilloy et al., 2017; Chaumard et al., 2018). FIB marks for Mg isotope analyses can be seen as squares at the surface of the grains (a-g). For T149/F1, SIMS pits for 6 oxygen isotope analyses (Defouilloy et al., 2017) and four Mg isotope analyses (this study; #1–4) are visible. Additional images can be found in Electronic Annex EA1.

pyroxene analyses, the same suite of RMs were used except for Mg and Si, which were calibrated using NMNH 122142 Kakanui augite. Probe for EPMA^{TM} (PFE) software was used for data reduction. Calculated detection limits (99% confidence) for the measured oxides in wt% were Na$_2$O-0.02, MgO-0.02, Al$_2$O$_3$-0.03, SiO$_2$-0.03, K$_2$O-0.02, CaO-0.02, TiO$_2$-0.05, Cr$_2$O$_3$-0.07, MnO-0.05, and FeO-0.06 wt%.

Endmembers of olivine and pyroxene are expressed as Fo (=Mg/[Mg + Fe] molar %) and En (=Mg/[Mg + Fe + Ca] molar %), respectively. We also report Wo (=Ca/[Mg + Fe + Ca] molar %) as the Ca endmember for pyroxene. The Fo, En, and Wo contents were calculated by considering total iron as ferrous iron.

3.2. FIB marking

All Wild 2 particles studied here have been previously analyzed by SIMS for oxygen isotope ratios (Nakashima

et al., 2012; Defouilloy et al., 2017; Chaumard et al., 2018) such that remaining areas for Mg isotope analyses were limited (typically 3×3 μm). In order to aim the primary ion beam precisely, we employed focused ion beam (FIB) marking to target areas prior to SIMS analyses (Nakashima et al., 2012; Defouilloy et al., 2017). FIB marking was performed with a field emission (FE) SEM equipped with a FIB system (Zeiss Auriga, UW-Madison), following procedures described in Defouilloy et al. (2017). After FIB marking, high-resolution SE images of all Wild 2 particles (Fig. 2 and Electronic Annex EA1) were obtained using the same instrument and were used for precise aiming of the primary ion beam.

3.3. Secondary ion mass spectrometry (SIMS)

Oxygen three-isotopes, Mg three-isotopes, and minor element analyses were performed with the WiscSIMS Cameca IMS 1280 equipped with the RF plasma ion source at UW-Madison. Five separate sessions (one for O isotopes, three for Mg isotopes, and one for minor elements) were conducted and analytical conditions were optimized for each session described below. Following analytical sessions, SIMS pits were investigated by SEM (S3400 at UW-Madison) or FE-SEM (LEO 1530 at UW-Madison), of which images are shown in Electronic Annex EA1-3.

3.3.1. SIMS oxygen isotope analyses

For oxygen three-isotope analyses of olivine from Kaba and DOM 08006 AOAs, the primary $^{133}Cs^+$ ion beam was focused to a ~8 μm diameter spot at 0.7 nA. Secondary oxygen ions ($^{16}O^-$, $^{17}O^-$, and $^{18}O^-$) were detected simultaneously using multi-collector Faraday cups (FCs) (Kita et al., 2010). To improve precision of $\delta^{17}O$ analyses, the FC for $^{17}O^-$ employed a high gain feedback resistor (10^{12} ohm) that can reduce thermal noise (Electronic Annex EA4-1). The other FCs for $^{16}O^-$ and $^{18}O^-$ employed 10^{10} ohm and 10^{11} ohm resistors, respectively. The mass resolving power (MRP) was set to ~2200 for $^{16}O^-$ and $^{18}O^-$, and 5000 for $^{17}O^-$. A single analysis took ~7 min, including 100 s of presputtering and baseline measurement, ~80 s for automated centering of secondary ion deflectors (DTFA-X, DTFA-Y), 200 s of integration (10 s × 20 cycles) of the secondary ion signals. At the end of each analysis, $^{16}O^1H^-$ was measured automatically to estimate the contribution of the tailing of $^{16}O^1H^-$ to the $^{17}O^-$ peak, which was always insignificant (<0.05‰ on $\delta^{17}O$; Electronic Annex EA4-1). A synthetic pure forsterite RM, HN-Ol ($\delta^{18}O = 8.90‰$: Kita et al., 2010), was used as the bracketing standard. The typical secondary $^{16}O^-$ ion intensity when measuring the HN-Ol was 7.5×10^8 counts per second (cps). Ten to fifteen unknown analyses were bracketed by 8 analyses of the HN-Ol standard (4 before and 4 after the unknowns). The external reproducibility of the HN-Ol standard was typically 0.4‰, 0.9‰, and 0.9‰ (2SD) for $\delta^{18}O$, $\delta^{17}O$, and $\Delta^{17}O$, respectively. The external reproducibilies (2SD) for each bracket are assigned as the uncertainties of bracketed unknown analyses. Instrumental biases in $\delta^{18}O$ were calibrated based on the bracket HN-Ol analyses. Since all olivine grains in AOAs analyzed are near-pure forsterite

(>Fo_{99}), no additional correction depending on Fo contents was applied.

3.3.2. SIMS magnesium isotope analyses

We conducted three sessions for Mg three-isotope analysis of olivine. For each session, the primary O_2^- ion beam was accelerated by 23 kV (–13 kV at the ion source and +10 kV at the sample surface) to the sample surface and secondary $^{24}Mg^+$, $^{25}Mg^+$, and $^{26}Mg^+$ ions were detected simultaneously using multi-collector FCs (L'2, C, and H1). Secondary ion optics are similar to those described in Kita et al. (2012) and Ushikubo et al. (2013). The MRP at 10% peak height was set to ~2500 and contributions of $^{48}Ca^+$ and $^{24}Mg^1H^+$ to $^{24}Mg^+$ and $^{25}Mg^+$ peaks, respectively, were negligibly small (EA2 in Fukuda et al., 2020). As described below, the primary beam intensity (and size) was optimized depending on the size of unknown samples, which led to different secondary Mg^+ ion intensities. Therefore, the combinations of resistors for the multi-collector FCs were optimized for each session. Each analysis duration was ~8–12 min, including 100 s of presputtering, ~100 s for automated centering of the secondary ion deflectors, and ~300–500 s of integration (10 s × 30 cycles for AOA analyses and 10 s × 50 cycles for Wild 2 analyses) of secondary ion signals. The baselines of the three FC detectors were monitored during each presputtering step, and their values were averaged over eight analyses.

Data reduction procedures follow those from Ushikubo et al. (2017). Terrestrial reference $^{25}Mg/^{24}Mg$ and $^{26}Mg/^{24}Mg$ values (0.12663 and 0.13932, respectively; Catanzaro et al., 1966) were used to convert raw-measured, background-corrected ratios to delta notation ($\delta^{25}Mg_m$ and $\delta^{26}Mg_m$). The $\delta^{25}Mg$ and $\delta^{26}Mg$ matrix effects were calibrated based on analyses of ~13 olivine reference materials (RMs), of which Mg isotope ratios in DSM-3 scale (Galy et al., 2003) have been determined by solution nebulization multi-collector inductively coupled plasma mass spectrometry (SN-MC-ICP-MS) or laser ablation MC-ICP-MS (Fukuda et al., 2020). Recently, we found complex matrix effects related to SIMS Mg isotope analyses of olivine, leading to instrumental biases on $\delta^{25}Mg$ that could not be fit by a simple regression to Fo contents. Instead, we apply a calibration that uses a combination of Mg^+/Si^+ signal ratios and Fo contents of olivine (Fukuda et al., 2020). Specifically, instrumental biases are estimated as a function of X = ($^{24}Mg^+/^{28}Si^+$)/Fo, where ($^{24}Mg^+/^{28}Si^+$) is the secondary ion $^{24}Mg^+/^{28}Si^+$ ratio obtained from SIMS minor element analysis (see section 3.3.3) and where Fo contents of unknown samples were obtained with TEM-EDX (Wild 2 olivine; Joswiak et al., 2012; Nakashima et al., 2012; Defouilloy et al., 2017; Chaumard et al., 2018) or FE-EPMA (AOA olivine; this study).

Magnesium isotope ratios of unknowns are reported as $\delta^{25}Mg$ and $\delta^{26}Mg$ values in DSM-3 scale. The bias corrected $\delta^{25}Mg$ and $\delta^{26}Mg$ values are calculated as follows:

$$\delta^i Mg = [(1 + \delta^i Mg_m/1000)/(1 + \delta^i Mg_{bias}/1000) - 1] \times 1000$$

where $i = 25$ or 26 and $\delta^i Mg_{bias}$ is the instrumental bias determined from the calibration curve (Electronic Annex

EA5). Uncertainties in $\delta^{25}Mg$ and $\delta^{26}Mg$ are estimated by combining the analytical uncertainties and error of the fit to the instrumental bias correction. More details for the estimation of uncertainties are summarized in Electronic Annex EA5.

The mass-independent raw-measured $\Delta^{26}Mg_m$ is defined as $\Delta^{26}Mg_m = [(1 + \delta^{26}Mg_m/1000)/(1 + \delta^{25}Mg_m/1000)^{1/\beta} - 1] \times 1000$. We assume that natural and instrumental mass-dependent fractionations follow a power law function, where an applied β value of 0.5128 was determined by vacuum evaporation experiments on melts of a Type B CAI bulk composition (Davis et al., 2015). $\Delta^{26}Mg_m$ values of olivine RMs obtained in the same analysis session were used to correct the non-mass dependent instrumental bias (see more details in Electronic Annex EA5). The mass-independent, bias-corrected $\Delta^{26}Mg$ of unknowns is defined as follows:

$$\Delta^{26}Mg = [(1 + \Delta^{26}Mg_{m(unknown)}/1000)/$$
$$(1 + \Delta^{26}Mg_{m(RM)}/1000) - 1] \times 1000$$

where $\Delta^{26}Mg_{m\,(unknown)}$ and $\Delta^{26}Mg_{m\,(RM)}$ are $\Delta^{26}Mg_m$ of unknowns and $\Delta^{26}Mg_m$ of olivine RMs, respectively. Finally, $\delta^{26}Mg^*$ of unknowns are estimated as: $\delta^{26}Mg^* = \Delta^{26}Mg \times (1 + \delta^{25}Mg/1000)^{1/\beta}$ (Ushikubo et al., 2017). We note that natural mass-dependent fractionations in Wild 2 and AOA olivines may not follow this power law β value, but that any potential $\delta^{26}Mg^*$ inaccuracy this causes is likely to be minimal. For example, if assuming kinetic Mg isotope fractionation ($\beta = 0.511$; Young and Galy, 2004), the $\delta^{26}Mg^*$ of Wild 2 and AOA olivines only change by a maximum of 0.03‰ within $\delta^{25}Mg$ values ranging from –3.8 to 0.6‰. This small offset is well within our analytical uncertainties ($\sim$0.05–0.47‰, 2SD).

The Wild 2 olivine particles were analyzed in session 1 (S1; 2018 Oct). The primary O_2^- beam was focused to 2 μm at 24 pA. All three FCs employed 10^{12} ohm resistors for detection of $^{24,25,26}Mg^+$ ions. Prior to each analysis, secondary $^{25}Mg^+$ ion images of the Wild 2 olivine particles were obtained by rastering the primary ion beam (24 pA) over a 10 μm × 10 μm area in order to identify the location of FIB marks. For this mode of operation, the secondary $^{25}Mg^+$ ions were detected with a multi-collector electron multiplier (EM; L1) by applying X-deflection after the secondary magnet (DSP2X), which is similar to previous techniques for oxygen and magnesium isotope analyses of Wild 2 particles (Nakashima et al., 2012, 2015; Defouilloy et al., 2017). One to four analyses were performed for each Wild 2 particle, bracketed by eight analyses of the San Carlos olivine (hereafter SC-Ol) grains mounted in the same disks. In addition, twelve other olivine RMs were measured for instrumental bias corrections (Electronic Annex EA4-2-1). The typical $^{24}Mg^+$ count rate during measurement of SC-Ol was 4.6×10^6 cps. The standard deviations of FC baselines over eight analyses were typically 120 cps for L'2, 90 cps for C, and 110 cps for H1, corresponding to 3×10^{-5} relative to $^{24}Mg^+$ and 1.6×10^{-4} relative to $^{25}Mg^+$ and $^{26}Mg^+$ ion intensities. In this session, we estimated the time constant of each 10^{12} ohm feedback resistor by monitoring the decay of secondary $^{24,25,26}Mg^+$ signals (i.e., after turning off the primary beam) from SC-Ol (Electronic Annex

EA4-5). The time constants of the three 10^{12} ohm feedback resistors range from 0.49 to 0.74 seconds, which are similar to each other. Thus we did not apply any tau corrections (e.g., Pettke et al., 2011). The external reproducibilities (2SD) of $\delta^{25}Mg_m$, $\delta^{26}Mg_m$, and $\Delta^{26}Mg_m$ for the SC-Ol bracket standard were 0.25‰, 0.26‰ and 0.47‰, respectively. The final uncertainties including error of the fit to the instrumental bias correction were typically 0.58‰ 1.05‰, and 0.54‰ for $\delta^{25}Mg$, $\delta^{26}Mg$, and $\delta^{26}Mg^*$, respectively.

Olivine grains from Kaba AOA (K27) were analyzed in session 2 (S2; 2018 Oct). The primary O_2^- beam was focused to 10 μm at 2 nA. The FC for $^{24}Mg^+$ (L'2) employed a 10^{10} ohm resistor, and the other two FCs for $^{25}Mg^+$ and $^{26}Mg^+$ (C and H1) employed 10^{11} ohm resistors. SC-Ol grains were used as a bracketing standard. In addition, five Mg-rich olivine RMs ($>$Fo$_{94}$) listed in Electronic Annex EA4-2-2 were measured for instrumental bias corrections. The typical $^{24}Mg^+$ count rate for SC-Ol was 4.4×10^8 cps. The external reproducibilities (2SD) of $\delta^{25}Mg_m$, $\delta^{26}Mg_m$, and $\Delta^{26}Mg_m$ for the SC-Ol bracket standard were 0.08‰, 0.15‰ and 0.05‰, respectively. The final uncertainties including error of the fit to the instrumental bias correction were typically 0.31‰, 0.60‰, and 0.06‰ for $\delta^{25}Mg$, $\delta^{26}Mg$, and $\delta^{26}Mg^*$, respectively.

Olivine grains from DOM 08006 AOAs were analyzed in session 3 (S3; 2018 Dec). The primary O_2^- beam was focused to $\sim$5 μm at 160 pA. As for Wild 2 analyses, all three FCs employed 10^{12} ohm resistors for detection of $^{24,25,26}Mg^+$ ions. SC-Ol grains were used as a bracketing standard. An additional 11 olivine RMs, listed in Electronic Annex EA4-2-3, were measured for instrumental bias corrections. The typical $^{24}Mg^+$ count rate when measuring SC-Ol was 3.0×10^7 cps. External reproducibilities (2SD) of $\delta^{25}Mg_m$, $\delta^{26}Mg_m$, and $\Delta^{26}Mg_m$ for the SC-Ol bracket standard were 0.13‰, 0.22‰ and 0.19‰, respectively. The final uncertainties including error of the fit to the instrumental bias correction were typically 0.44‰ 0.88‰, and 0.23‰ for $\delta^{25}Mg$, $\delta^{26}Mg$, and $\delta^{26}Mg^*$, respectively.

3.3.3. SIMS Mg^+/Si^+ ratios and minor element analyses

Mg^+/Si^+ ratios and minor element (Ca, Cr, Mn, and Fe) concentrations were obtained using the same analytical conditions reported in Fukuda et al. (2020). Secondary $^{24}Mg^+$ ions were detected by an axial FC (FC2) with a 10^{11} ohm resistor. The other secondary ions ($^{23}Na^+$, $^{27}Al^+$, $^{28}Si^+$, $^{40}Ca^+$, $^{52}Cr^+$, $^{55}Mn^+$, $^{56}Fe^+$, and $^{60}Ni^+$), as well as mass 22.7 (used for stabilizing the magnetic field for $^{23}Na^+$), were detected by an axial EM that operated in magnetic peak jumping mode. Due to consumption of sample area from prior O and Mg isotope analyses of the Wild 2 olivine particles, we focused the primary O_2^- beam down to 1.5 μm in diameter (6 pA) and aimed it inside the previous SIMS pits ($\sim$2 μm in diameter) from Mg isotope analyses. For AOAs from DOM 08006, the primary ion beam was also aimed inside previous SIMS pits ($\sim$5 μm in diameter) from Mg isotope analyses. Prior to each analysis, a secondary $^{24}Mg^+$ ion image of the targeted SIMS pit was obtained by rastering the primary ion beam (6 pA) over a 10 × 10 μm area in order to aim the primary

ion beam inside the SIMS pit. The AOA (K27) from Kaba had abundant areas for minor element analyses so that flat surface areas near the previous SIMS pits from Mg isotope analyses were analyzed. SC-Ol grains were used as a running standard. An additional 12 olivine standards (Electronic Annex EA4-3) were also measured to obtain $^{24}Mg^+/^{28}Si^+$ ratios and to determine relative sensitivity factors (RSFs) of minor elements (Ca, Cr, Mn, and Fe). The typical $^{24}Mg^+$ count rate for SC-Ol was $\sim7.6 \times 10^5$ cps. We also conducted multiple analyses of olivine RMs in order to compare the instrumental bias within previously generated SIMS pits and flat surface areas (see more details in Electronic Annex EA5). A single analysis was ~6 min in duration, including 100 s of presputtering, $\sim$80 s for automated centering of secondary ion deflectors, and 160 s of integration (32 s × 5 cycles) of secondary ion signals. Detection limits were evaluated based on the measurement of synthetic pure forsterite RM (HN-Ol), which is expected not to contain Ca, Cr, Mn, and Fe. The detection limits of CaO, Cr_2O_3, MnO, and FeO were 0.002, 0.0001, 0.001, and 0.003 wt%, respectively.

4. RESULTS

4.1. AOA petrography and mineral chemistry

One AOA (K27) from Kaba and eight AOAs (501, 502, 503, 505, 511, 512, 513, and 514) from DOM 08006 were studied by SEM-EDS and FE-EPMA. All nine AOAs are composed of forsteritic olivine, opaque minerals (Fe,Ni-metal and/or weathering products), and Ca-, Al-rich portions (±spinel, ±anorthite, and Al-(Ti)-diopside). Low-Ca pyroxene is rare and was identified in two out of nine AOAs (502 and 503). The mineralogical characteristics of the nine AOAs are summarized in Table 1. The AOAs studied here are less than $\sim$400 µm, except for K27 from Kaba ($\sim$1.7 mm). Average elemental compositions (wt%) and Fo, En, and Wo contents of AOA minerals are summarized in Table 2. Individual EPMA data and their analysis locations are summarized in Electronic Annex EA4-4 and EA6, respectively. Olivine grains from the nine AOAs have a

narrow range of Fo content (Fo_{99-100}). CaO, Cr_2O_3, MnO, and FeO contents of olivine grains vary by $\sim$0.4, $\sim$0.5, $\sim$0.5, and $\sim$1.1 wt%, respectively. As we discuss later, FeO contents obtained with EPMA analyses might be overestimated due to secondary fluorescence effects (e.g., Fournelle et al., 2005; Buse et al., 2018) from surrounding FeO enhanced phases. En components of diopside in K27, 505, 511, and 513 range from 44.0 to 50.2. Al_2O_3 and TiO_2 contents of these diopside grains range from 3.4 to 11.9 wt% and 0.2 to 2.9 wt%, respectively.

The AOAs investigated show variations in abundances of pores, shapes of external margins and ratios of minor minerals to olivine (Figs. 3–5). Three (K27, 505 and 513) show a compact texture with little porosity in the forsterite-rich regions (Fig. 3). The other AOAs (e.g., 502 and 503) are more porous and are irregularly shaped (Figs. 4 and 5). Detailed information for each inclusion is summarized below.

AOA K27 from Kaba is the largest aggregate ($\sim$1.7 mm; Fig. 3a) studied here. It consists of multiple nodules, and each nodule is composed of Ca-, Al-rich domains enclosed by sinuous forsterite ($Fo_{99.5-100}$) and opaque minerals (Fig. 3b). Forsterite regions display dense textures with little porosity between grain boundaries (Fig. 3b and c). Ca-, Al-rich domains have anorthite ± spinel cores rimmed by Al-diopside (Fig. 3c). Spinel grains are anhedral and appear corroded by the surrounding anorthite (Fig. 3c). Al-diopside occurs between anorthite and forsterite (Fig. 3b and c).

AOA 513 from DOM 08006 (Fig. 3d) consists of multiple Ca-, Al-rich portions enclosed by nearly pure forsterite grains ($Fo_{99.5-99.7}$) and rare Fe,Ni-metal. This AOA has anorthite ± anhedral spinel cores rimmed by Al-diopside, which are enclosed by dense forsterite (Fig. 3e). Al-diopside occurs between anorthite and forsterite (Fig. 3e). The mineralogy and texture of this AOA are similar to those of Kaba AOA K27 (Fig. 3b and c).

AOA 505 from DOM 08006 (Fig. 3f) consists of spinel-diopside-rich nodules enclosed by dense forsterite ($Fo_{99.7-99.9}$) with minor Fe,Ni-metal. This inclusion may also be classified as a CAI with a thick forsterite rim. Spinel

Table 1
Mineralogy of AOAs from Kaba (CV3.1) and DOM 08006 (CO3.01) carbonaceous chondrites.

Chondrite	AOA name	AOA texture	fo	FeNi	Ca-, Al-rich portions				LIME ol[b]	lpx
					Al-(Ti)-di	an	sp	halo[a]		
Kaba	K27	Compact	+	+	+	+	+	–	–	–
DOM 08006	501	Pore-rich	+	+	+	+	–	+	+	–
DOM 08006	502	Pore-rich	+	+	+	+	–	+	+	+
DOM 08006	503	Pore-rich	+	+	+	+	–	+	+	+
DOM 08006	505	Compact	+	+	+	–	+	–	+	–
DOM 08006	511	Pore-rich	+	+	+	+	–	+	+	–
DOM 08006	512	Pore-rich	+	+	+	+	–	+	+	–
DOM 08006	513	Compact	+	+	+	+	+	–	–	–
DOM 08006	514	Pore-rich	+	+	+	+	–	+	–	–

fo = forsterite, FeNi = Fe,Ni-metal and/or weathering products, Al-(Ti)-di = Al-(Ti)-diopside, an = anorthite, sp = spinel, LIME ol = LIME olivine, lpx = low-Ca pyroxene.

[a] Diffuse area that appears to be brighter in BSE images than surrounding forsterite. See Section 4.1.

[b] Olivine grains with MnO/FeO (wt%) ≥ 1. The MnO/FeO ratios are calculated from SIMS data in Table 4, except for AOA 514. The MnO/FeO ratios of olivine grains from AOA 514 are calculated from FE-EPMA data due to an absence of SIMS minor element data.

Table 2
Fo, En, and Wo contents and average elemental compositions (wt%) of minerals in Kaba and DOM 08006 AOAs obtained with electron microprobe.

Chondrite	AOA name	Mineral[a]	Fo[b]	1SD	En[b]	1SD	Wo[b]	1SD	No. of analyses	Na₂O	MgO	Al₂O₃	SiO₂	K₂O	CaO	TiO₂	Cr₂O₃	MnO	FeO	Total
Kaba	K27	fo	99.9	0.1					15	b.d.	57.17	0.06	42.31	b.d.	0.15	0.06	0.20	0.10	0.19	100.23
Kaba	K27	hpx			48.9	1.4	51.1	1.4	2	b.d.	17.15	5.32	50.88	b.d.	24.88	1.94	0.11	b.d.	b.d.	100.29
DOM 08006	501	fo	99.5	0.3					12	b.d.	57.04	0.06	42.24	b.d.	0.19	0.05	0.16	0.11	0.49	100.34
DOM 08006	502	fo	99.5	0.2					7	b.d.	57.14	0.05	42.35	b.d.	0.07	0.10	0.34	0.27	0.48	100.81
DOM 08006	503	fo	99.7	0.1					7	b.d.	57.61	0.05	42.50	b.d.	0.09	0.06	0.22	0.10	0.34	100.96
DOM 08006	505	fo	99.8	0.1					7	b.d.	57.56	0.04	42.15	b.d.	0.11	0.06	0.20	0.12	0.18	100.41
DOM 08006	505	hpx			50.1		49.6	0.2	3	b.d.	18.12	3.87	53.00	b.d.	24.92	0.28	0.09	b.d.	0.20	100.48
DOM 08006	511	fo	99.5	0.1					7	b.d.	57.36	0.04	42.17	b.d.	0.12	0.05	0.13	0.16	0.54	100.56
DOM 08006	511	hpx			45.1	1.6	54.3	1.4	2	b.d.	14.90	10.17	47.95	b.d.	24.90	2.07	0.10	b.d.	0.35	100.44
DOM 08006	511	an							1	0.03	0.55	35.94	42.55	b.d.	19.84	0.07	0.08	b.d.	0.37	99.43
DOM 08006	512	fo	99.7	0.1					7	b.d.	57.35	0.08	42.32	b.d.	0.09	0.08	0.27	0.15	0.27	100.61
DOM 08006	513	fo	99.6	0.1					7	b.d.	57.32	0.04	42.44	b.d.	0.33	0.05	0.10	b.d.	0.40	100.69
DOM 08006	513	hpx			47.9		51.4	1.2	4	b.d.	16.63	6.85	50.15	b.d.	24.83	1.38	0.10	b.d.	0.46	100.40
DOM 08006	514	fo	99.7	0.2					7	b.d.	57.40	0.07	42.36	b.d.	0.35	0.07	0.07	b.d.	0.33	100.65

[a] fo = forsterite, hpx = high-Ca pyroxene, an = anorthite.
[b] Fo = Mg/(Mg + Fe) molar %, En = Mg/(Mg + Fe + Ca) molar %, Wo = Ca/(Mg + Fe + Ca) molar %.

is separated from forsterite by a layer of Al-diopside (Fig. 3g).

AOA 502 from DOM 08006 is irregularly shaped and porous (Fig. 4a), consisting mostly of forsterite (Fo$_{99.3-99.7}$), with minor Fe,Ni-metal and numerous irregularly shaped diffuse areas (Fig. 4b–d). Rare low-Ca pyroxene is also observed (Fig. 4b and d), and forsterite regions of this AOA are porous (Fig. 4b and c). SEM-EDS analyses indicate that the diffuse areas are mixtures of tiny Al-diopside grains, and forsterite. Such diffuse areas are also observed in AOAs from ALHA77307 (CO3.03) as brighter areas in BSE images than surrounding forsterite, referred to as haloes by Sugiura et al. (2009). Forsterite grains within this AOA have the highest MnO abundances (∼0.5 wt%) among the nine AOAs studied here.

AOA 503 from DOM 08006 is a fine-grained, porous object (Fig. 4e), consisting mostly of forsterite (Fo$_{99.4-99.8}$), with minor Fe,Ni-metal and numerous irregularly shaped Ca-, Al-rich portions (tiny Al-diopside grains and an anorthitic halo; Fig. 4f). Rare low-Ca pyroxene is also observed (Fig. 4g). The mineralogy and texture of this AOA is similar to those of AOA 502, but MnO contents of forsterite grains are lower (∼0.1 wt%).

AOA 501 from DOM 08006 (Fig. 5a) consists of forsterite (Fo$_{99.0-99.9}$), Fe,Ni-metal, and numerous irregularly shaped, fine-grained Ca, Al-rich portions. Most of this AOA is composed of porous forsterite with numerous irregularly shaped, fine-grained Ca, Al-rich portions (Fig. 5b). However, a region shown in Fig. 5c is less porous, and has nodule-like (Ca-, Al-rich core and sinuous forsterite) textures, similar to characteristics observed in Kaba AOA K27 (e.g., Fig. 3b).

AOAs 511 and 512 from DOM 08006 are irregularly shaped objects (Fig. 5d and 5e, respectively), consisting of forsterite (Fo$_{99.3-99.6}$), Ca-, Al-rich portions (Al-diopside and anorthite), and minor Fe,Ni-metal. Ca, Al-rich diffuse areas (haloes) are observed in each AOA.

AOA 514 from DOM 08006 is a sub-rounded object (Fig. 5f), consisting of forsterite (Fo$_{99.2-99.9}$) and irregularly shaped Ca-, Al-rich portions (Al-diopside and anorthite) that are concentrated in the inner part of the AOA. Forsterite grains of the inner part of the AOA, along with Ca, Al-rich portions, are more porous relative to the outer regions of this AOA.

4.2. Oxygen isotope ratios of AOA olivines

We obtained 32 olivine oxygen isotope ratio data from eight of the nine AOAs studied here (the exception being AOA 512, due to small olivine grains). $\delta^{18}O$, $\delta^{17}O$, and $\Delta^{17}O$ values are reported in Table 3. Raw-measured O isotope ratios of AOA olivines are reported in Electronic Annex EA4-1. As shown in Fig. 6a, oxygen isotope ratios of all measured AOA olivines are ^{16}O-rich ($\Delta^{17}O \leq -23$‰) and plot either on the Primitive Chondrule Mineral (PCM; Ushikubo et al., 2012, 2017) line or between the PCM and CCAM (Carbonaceous Chondrite Anhydrous Mineral; Clayton et al., 1977) lines. Individual olivine analyses from the eight AOAs have limited variations in $\delta^{18}O$ and $\Delta^{17}O$ values, ranging from –44.0‰ to –47.4‰
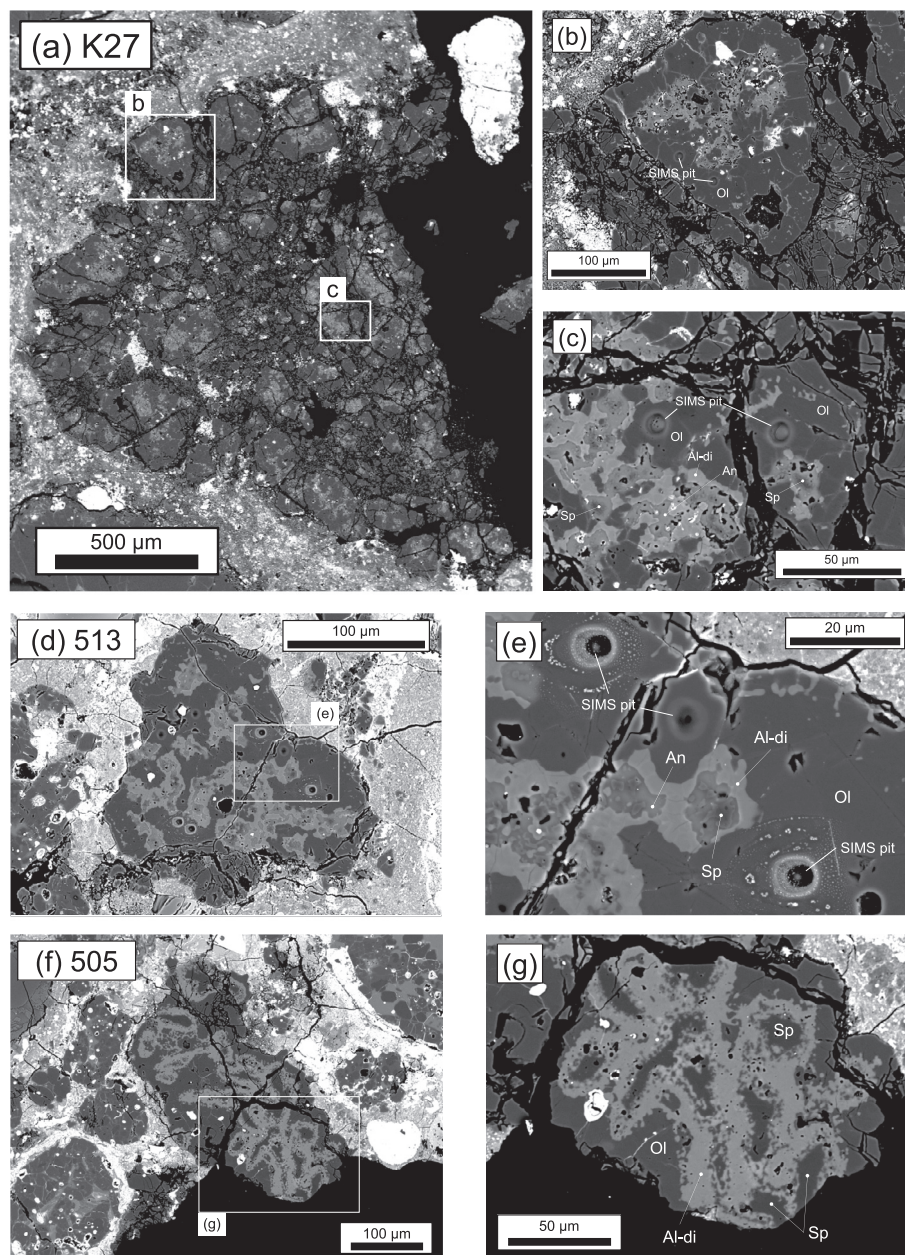
Fig. 3. BSE images of compact AOAs from Kaba and DOM 08006. (a–c) K27 from Kaba, (d–e) 513 from DOM 08006, (f-g) 505 from DOM 08006. Mineral phases shown are olivine (Ol), anorthite (An), spinel (Sp) and Al-diopside (Al-di).

and –23.0‰ to –24.8‰, respectively. Subtle variations of oxygen isotope ratios are observed within each AOA (e.g., K27 and 514; Fig. 6a), but averaged oxygen isotope ratios of individual AOAs form a tight cluster on the PCM line (Fig. 6b), and are identical within uncertainties.

4.3. Magnesium isotope ratios of AOA and Wild 2 olivines

We obtained 36 olivine magnesium three-isotope ratio data from eight of the nine AOAs studied here. We did not acquire Mg isotope data from AOA 514 because large secondary deflector values (DTFA values >50) had to be applied, and under such a condition δ^{25}Mg analyses are

inaccurate due to additional instrument fractionation. Magnesium isotope ratios (δ^{25}Mg and δ^{26}Mg) are listed in Table 4 and plotted in Fig. 7. Individual SIMS data including raw-measured Mg isotope ratios are reported in Electronic Annex EA4-2-6 and EA4-2-7. δ^{25}Mg values of AOA olivines range from –3.8 ± 0.5‰ (2σ) to –0.2 ± 0.3‰ (2σ). All Mg isotope analyses obtained in AOA olivines show a linear correlation between δ^{26}Mg and δ^{25}Mg (Fig. 7a). We also calculated logarithmic values (δ^{25}Mg′ and δ^{26}Mg′) that are converted from δ^{25}Mg and ^{26}Mg values using the following formula: δ^{i}Mg′ $= 1000 \times \ln$ $(1 + \delta^{i}$Mg/1000) (Electronic Annex EA4-2-8). The logarithmic values are used to determine
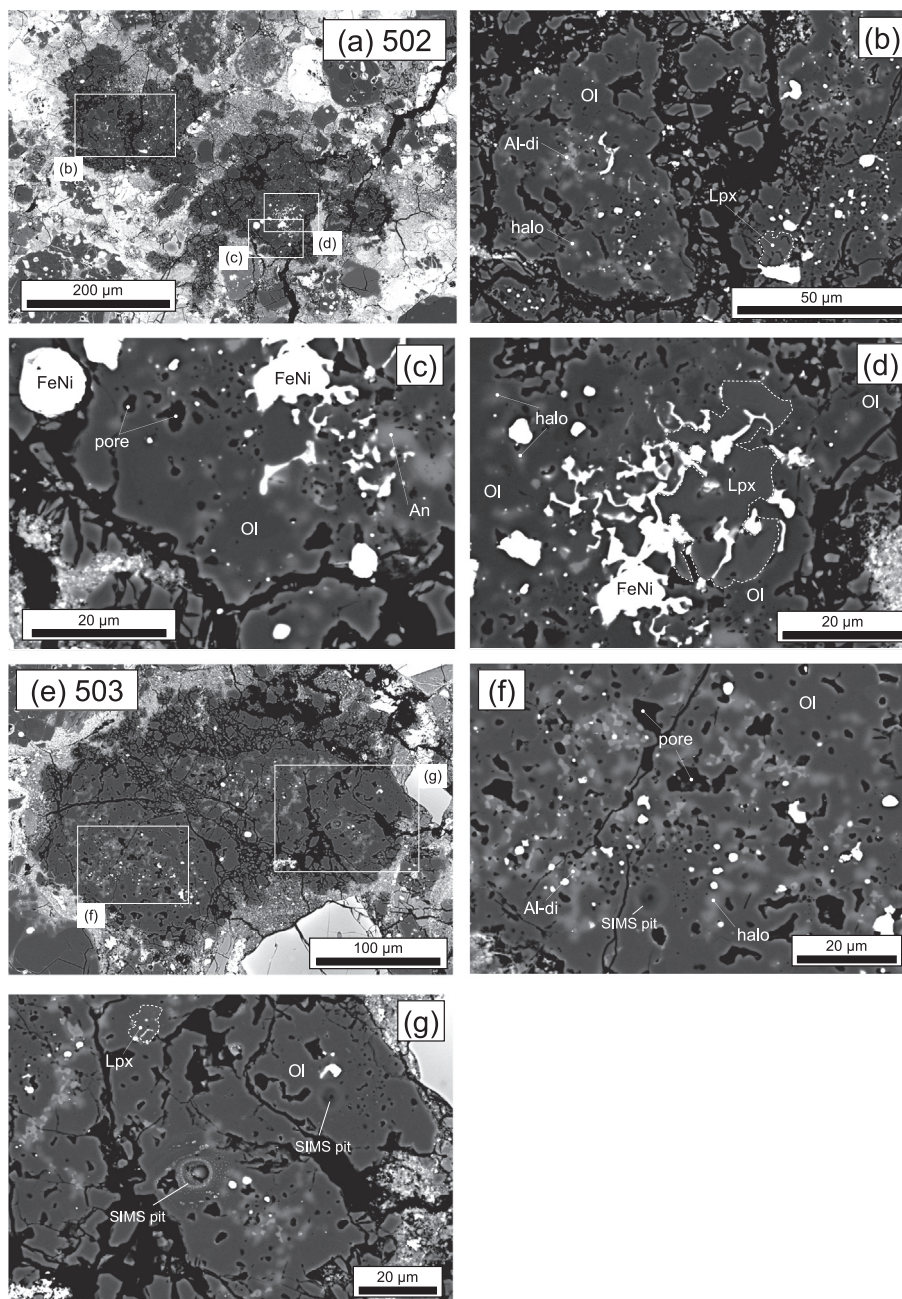
Fig. 4. BSE images of pore-rich, low-Ca pyroxene-bearing AOAs from DOM 08006. (a–d) 502, (e–g) 503. Mineral phases shown are olivine (Ol), low-Ca pyroxene (Lpx), Al-diopside (Al-di), anorthite (An) and Fe,Ni-metal (FeNi). Pores, and haloes that represent diffuse area consisting of mixtures of tiny Al-diopside grains and forsterite, are indicated.

the slope and intercept in $\delta^{26}Mg'$ versus $\delta^{25}Mg'$ space (Fig. 8), with values of 0.516 ± 0.012 (2σ) and -0.06 ± 0.04 (2σ), respectively (using Isoplot 4.15 model 1; Ludwig, 2012). Variation in $\delta^{25}Mg$ and $\delta^{26}Mg$ within each AOA is identified, which follows a line with the same slope of 0.516 (Fig. 7b–i). Among them, $\delta^{25}Mg$ and $\delta^{26}Mg$ values of AOA 501 are bimodally distributed on the slope 0.516 line (Fig. 7c).

Magnesium isotope ratios ($\delta^{25}Mg$ and $\delta^{26}Mg$) of Wild 2 olivine particles T57/F10, T77/F4, T77/F50, T149/F1, and T175/F1 are listed in Table 5 and plotted in Fig. 9. Difficulties with the analyses of three Wild 2 particles (T77/F6, T77/F7, and T149/F11a) or data reduction problems prevented the reporting of bias-corrected $\delta^{25}Mg$ and $\delta^{26}Mg$ values. For analyses of T77/F6 and T77/F7, ($Mg^+/Si^+/$ Fo) values of these particles are outside the range of the instrumental fractionation calibration curve, meaning we could not properly correct data for instrumental mass fractionation. For T149/F11a, we observed that the Mg ion yields and $\delta^{25}Mg_m$ values changed significantly during the
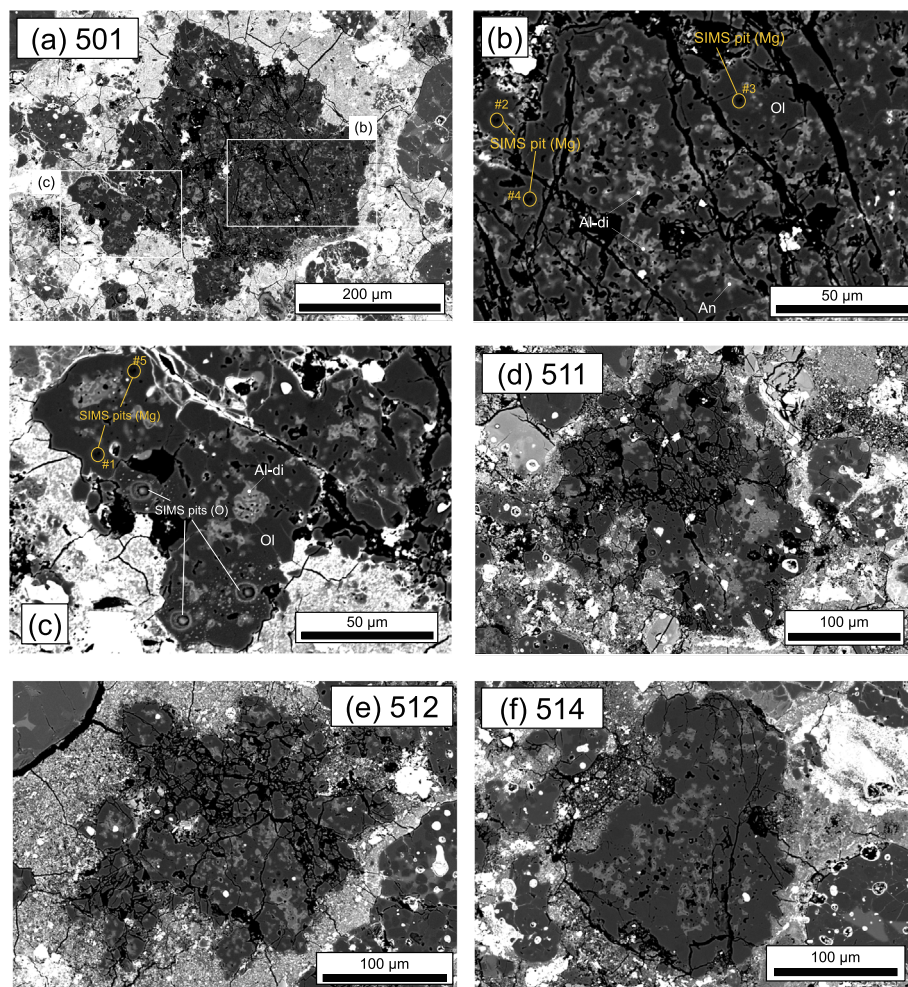
Fig. 5. BSE images of pore-rich AOAs from DOM 08006. (a) 501, (b) pore-rich lithology in 501, (c) compact lithology in 501, (d) 511, (e) 512, (f) 514. The locations of Mg isotope analyses for pore-rich and compact lithologies in AOA 501 are indicated in (b-c). Mineral phases shown are olivine (Ol), Al-diopside (Al-di) and anorthite (An).

analysis. These changes were not observed among olivine RM analyses, meaning we could not properly correct data for instrumental mass fractionation. More detailed explanations for these three particles can be found in Electronic Annex EA7. All individual data, including raw-measured Mg isotope ratios of the eight Wild 2 particles, are reported in Electronic Annex EA4-2-5. Regarding the five Wild 2 particles for which Mg isotope ratios were successfully determined, they show slight variations in δ^{25}Mg, ranging from $-1.0 \; ^{+0.4}/_{-0.5}$‰ (2σ) to $0.6 \; ^{+0.5}/_{-0.6}$‰ (2σ). The Mg isotopic data from these five Wild 2 particles fall on the same slope 0.516 line that is defined by individual AOA olivines (Fig. 9). Particles T77/F50 and T149/F1 were analyzed multiple times (N = 3 and N = 4, respectively) and do not show intra-grain variations in δ^{25}Mg and δ^{26}Mg values beyond uncertainties (Table 5 and Fig. 9).

δ^{26}Mg* values of AOA olivines and Wild 2 olivines are reported in Tables 4 and 5, respectively, and are plotted against their δ^{25}Mg values in Fig. 10. δ^{26}Mg* values of

AOA olivines from Kaba and DOM 08006 range from -0.15 ± 0.25‰ (2σ) to 0.17 ± 0.24‰ (2σ) and do not show resolvable excesses in ^{26}Mg when compared to inferred Solar System initial δ^{26}Mg* values (-0.040‰; Jacobsen et al., 2008 or -0.016‰; Larsen et al., 2011). δ^{26}Mg* values of Wild 2 olivines range from -0.41 ± 0.76‰ (2σ) to 0.31 ± 0.37‰ (2σ) and do not show resolvable excesses in ^{26}Mg.

4.4. Minor element abundances of AOA and Wild 2 olivines obtained with SIMS

CaO, Cr_2O_3, MnO and FeO contents in AOA and Wild 2 olivines were determined with a spatial resolution of ~1.5 μm by SIMS (Tables 4 and 5). Olivines from Kaba and DOM 08006 AOAs show one or two orders of magnitude variation in CaO, Cr_2O_3, and MnO contents ranging from 0.03 to 0.28 wt%, 0.06 to 0.32 wt%, and 0.004 to 0.31 wt%, respectively. FeO contents in olivines from DOM 08006 AOAs do not show significant variation

Table 3
Oxygen isotope ratios of AOA olivines from Kaba and DOM 08006.

Sample/Location #[a]			$\delta^{18}O$ (‰)	Unc. (2σ)	$\delta^{17}O$ (‰)	Unc. (2σ)	$\Delta^{17}O$ (‰)	Unc. (2σ)
Kaba (CV3.1)								
	K27							
		#1	−44.6	0.5	−47.0	0.9	−23.8	1.0
		#2	−45.1	0.5	−47.2	0.9	−23.7	1.0
		#3	−44.0	0.5	−46.8	0.9	−24.0	1.0
		#4	−45.2	0.5	−47.2	0.9	−23.7	1.0
		#5	−45.7	0.5	−46.8	0.9	−23.0	1.0
		#6	−45.4	0.5	−47.1	0.9	−23.5	1.0
		#7	−45.6	0.4	−48.2	0.7	−24.5	0.7
		#8	−45.1	0.4	−48.1	0.7	−24.7	0.7
		#9	−45.6	0.4	−48.3	0.7	−24.6	0.7
		#10	−46.1	0.4	−47.7	0.7	−23.7	0.7
		Average & 2SD	−45.2	1.2	−47.5	1.2	−23.9	1.1
DOM 08006 (CO3.01)								
	501							
		#1	−46.4	0.2	−47.4	0.9	−23.3	0.8
		#2	−45.7	0.2	−47.7	0.9	−23.9	0.8
		#3	−46.2	0.2	−47.9	0.9	−23.9	0.8
		#4	−45.9	0.2	−48.1	0.9	−24.2	0.8
		#5	−46.5	0.2	−47.7	0.9	−23.5	0.8
		Average & 2SD	−46.1	0.7	−47.8	0.5	−23.8	0.7
	502							
		#1	−46.2	0.2	−48.2	0.9	−24.2	0.8
	503							
		#1	−45.9	0.2	−47.5	0.9	−23.7	0.8
	505							
		#1	−46.5	0.4	−48.0	0.7	−23.8	0.7
		#2	−45.9	0.4	−47.3	0.7	−23.5	0.7
		#3	−46.4	0.4	−48.1	0.7	−24.0	0.7
		Average & 2SD	−46.3	0.7	−47.8	0.8	−23.8	0.5
	511							
		#1	−45.4	0.4	−47.7	0.7	−24.1	0.7
	513							
		#1	−45.5	0.2	−48.0	0.9	−24.3	0.8
		#2	−46.0	0.2	−48.3	0.9	−24.4	0.8
		#3	−45.9	0.2	−47.7	0.9	−23.9	0.8
		#4	−45.6	0.2	−47.5	0.9	−23.8	0.8
		Average & 2SD	−45.8	0.4	−47.9	0.7	−24.1	0.6
	514							
		#1	−45.5	0.4	−47.7	0.7	−24.0	0.7
		#2	−45.9	0.4	−47.7	0.7	−23.8	0.7
		#3	−45.8	0.4	−48.1	0.7	−24.3	0.7
		#4	−47.4	0.4	−49.1	0.7	−24.5	0.7
		#5	−45.5	0.4	−47.9	0.7	−24.2	0.7
		#6	−45.6	0.4	−48.6	0.7	−24.8	0.7
		#7	−45.8	0.4	−47.9	0.7	−24.1	0.7
		Average & 2SD	−45.9	1.3	−48.1	1.1	−24.3	0.7

[a] Analysis points are shown in Electronic Annex EA2.

among the seven examples investigated (0.03–0.08 wt%; Fig. 11). In contrast, olivines from Kaba AOA K27 are more variable (0.06–0.58 wt%) than DOM 08006 AOAs (Fig. 11). MnO/FeO (wt%) ratios of 38 olivine analyses show a large variation (0.1–4.2) even within a single inclusion (e.g., 0.1–2.1 in AOA511; see Table 4).

CaO, Cr_2O_3, and MnO contents in five Wild 2 olivine particles (T57/F10, T77/F4, T77/F50, T149/F1, and T175/F1) range from 0.004 to 0.19 wt%, 0.07 to 0.53 wt%, and 0.06 to 0.66 wt%, respectively. The ^{16}O-depleted, FeO-rich Wild 2 olivines (T77/F4 and T149/F1) have higher CaO contents (0.12–0.19 wt%) than the ^{16}O-rich,
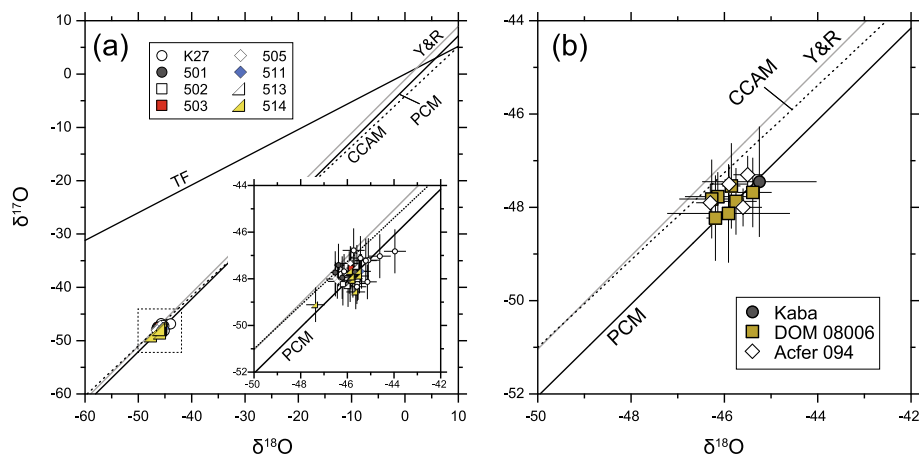
Fig. 6. Oxygen three-isotope ratios of the eight AOA olivines from Kaba (K27) and DOM 08006 (501, 502, 503, 505, 511, 513, 514). All measured data (=individual olivine analyses) are shown in (a). The insert in (a) shows detail of the analyses highlighted by the dotted box. Average $\delta^{17,18}O$ values of each AOA are shown in (b), though for three AOAs (502, 503, 511) only a single analysis was collected. For comparison, data for AOAs from Acfer 094 (Ushikubo et al., 2017) are also shown in (b). Reference lines are the terrestrial fractionation (TF), the carbonaceous chondrite anhydrous mineral (CCAM), the Young and Russell (Y&R), and the primitive chondrule mineral (PCM) lines. Errors are 2SD for data obtained in this study. Errors for Acfer 094 data are propagated, as described in Ushikubo et al. (2017).

FeO-poor Wild 2 olivines (0.004–0.04 wt%). The MnO/FeO (wt%) ratio of ^{16}O-rich olivine from T77/F50 is 3.8, is consistent with LIME olivine (Klöck et al., 1989). The MnO/FeO (wt%) ratios of the other ^{16}O-rich olivines (T57/F10 and T175/F1) are 0.38 and 0.37, respectively. ^{16}O-depleted Wild 2 olivines T77/F4 and T149/F1 have very low MnO/FeO ratios (≤ 0.03) due to their abundant FeO contents.

5. DISCUSSION

5.1. Distribution of O isotopes at the AOA-forming regions

Ushikubo et al. (2017) conducted O isotope analyses of individual AOA minerals from the Acfer 094 (C-ungrouped 3.00) carbonaceous chondrite and observed subtle variations in O isotope ratios along slope ∼1 lines (CCAM and PCM). Some AOA olivines studied here show similar detectable variability (Fig. 6a), indicating slight oxygen isotope variation of early solar nebular gas (Ushikubo et al., 2017). However, these variations are very small compared to the differences between O isotope ratios of AOAs and more ^{16}O-depleted objects (e.g., chondrules). In fact, the averaged O isotope ratios of individual AOAs from Kaba and DOM 08006 cannot be distinguished from each other (Fig. 6b). Those of AOAs from Acfer 094 (Ushikubo et al., 2017) also plot within the range of Kaba and DOM 08006 AOAs (Fig. 6b). These observations indicate that AOAs from Kaba, DOM 08006, and Acfer 094 formed in a single ^{16}O-rich gaseous reservoir (average $\Delta^{17}O = -23.9 \pm 0.5‰$; 2SD; N = 12; Ushikubo et al., 2017 and this study), probably near the proto-Sun (Krot et al., 2004a,b) and were transported to accretion regions of each chondrite parent body.

In addition to AOAs, O isotope ratios of fine-grained CAIs from type 3.00–3.05 chondrites as well as spinel-hibonite inclusions (SHIBs) from CM chondrites are distributed between the CCAM and PCM lines with limited variations in $\Delta^{17}O$ from –24‰ to –22‰ (Köop et al., 2016; Ushikubo et al., 2017). Regarding $\Delta^{17}O$ values, CAIs from the least metamorphosed CO and CR chondrites also exhibit consistently ^{16}O-rich isotope characteristics ($\Delta^{17}O \leq -20‰$; Makide et al., 2009; Bodénan et al., 2014; Simon et al., 2019; Zhang et al., 2020). The O isotope similarity among refractory inclusions from thermally unmetamorphosed chondrites suggests that they formed in a homogeneously ^{16}O-rich reservoir.

5.2. Distribution of Mg isotopes at the AOA- and Wild 2 olivine-forming regions

We observe large variation in Mg isotopes of AOA olivine (Fig. 7). Other types of refractory inclusions (i.e., CAIs) also exhibit isotopic variations in multiple elements, including Mg (e.g., Liu et al., 2009; Wasserburg et al., 2012; MacPherson et al., 2017; Park et al., 2017), which are sometimes attributed to nucleosynthetic anomalies. However, a nucleosynthetic origin for the negative $\delta^{25}Mg$ and $\delta^{26}Mg$ values observed in AOA olivine seems unlikely because these values are linearly correlated with each other (Fig. 7), with a slope of ∼0.5. Instead, this correlation is most likely the result of mass-dependent isotope fractionation. Based on theoretical studies, equilibrium and kinetic mass-dependent processes have different slopes in $\delta^{26}Mg'$ versus $\delta^{25}Mg'$ space (0.521 and 0.511, respectively; Young and Galy, 2004; Davis et al., 2015). The slope of the mass-dependent fractionation observed in the AOA olivines studied here (0.516 $\pm$ 0.012, 2σ; Fig. 8) is in between these expected slopes, and therefore cannot be distinguished as being the result of an equilibrium or kinetic process.

Teng et al. (2010) conducted Mg isotope analyses of 38 chondrites which show indistinguishable ratios

Table 4
Magnesium isotope ratios and minor elemental abundances of AOA olivine from Kaba and DOM 08006 obtained with SIMS.

Sample/Location #[a]	$\delta^{25}Mg_{DSM-3}$ (‰)	Unc. (+/−) (2σ)		$\delta^{26}Mg_{DSM-3}$ (‰)	Unc. (+/−) (2σ)		$\delta^{26}Mg*$ (‰)	Unc. (2σ)	CaO (wt%)	Unc. (2σ)	Cr_2O_3 (wt%)	Unc. (2σ)	FeO (wt%)	Unc. (2σ)	MnO (wt%)	Unc. (2σ)	MnO/ FeO	Unc. (2σ)
Kaba (CV3.1)																		
K27																		
#3[b]	−0.39	0.30	0.31	−0.68	0.59	0.59	0.04	0.06	0.128	0.004	0.110	0.007	0.324	0.017	0.027	0.002	0.08	0.01
#4	−0.42	0.31	0.31	−0.78	0.60	0.60	−0.01	0.06	0.150	0.005	0.081	0.005	0.064	0.002	0.008	0.002	0.13	0.04
#5	−0.25	0.30	0.31	−0.48	0.59	0.59	−0.03	0.06	0.158	0.005	0.083	0.005	0.065	0.003	0.008	0.001	0.12	0.02
#6	−0.51	0.30	0.33	−0.95	0.59	0.62	0.00	0.06	0.230	0.022	0.057	0.004	0.116	0.003	0.009	0.001	0.08	0.01
#7	−0.64	0.31	0.31	−1.21	0.60	0.60	−0.01	0.06	0.202	0.017	0.113	0.007	0.072	0.003	0.024	0.001	0.34	0.02
#8	−0.69	0.31	0.31	−1.12	0.60	0.60	0.16	0.06	0.136	0.005	0.105	0.007	0.081	0.003	0.007	0.002	0.09	0.02
#9[b]	−0.23	0.32	0.32	−0.38	0.61	0.61	0.01	0.06	0.089	0.006	0.138	0.012	0.184	0.006	0.098	0.004	0.53	0.03
Average & 2SD	−0.45	0.35	0.35	−0.80	0.63	0.63	0.02	0.13	0.156	0.094	0.098	0.037	0.129	0.192	0.026	0.066	0.20	0.59
DOM 08006 (CO3.01)																		
501																		
#1_outer left part[c]	−0.42	0.44	0.44	−0.55	0.87	0.87	0.17	0.24	0.119	0.003	0.188	0.006	0.072	0.003	0.088	0.001	1.21	0.06
#2	−3.31	0.44	0.44	−6.27	0.86	0.86	0.09	0.24	0.082	0.002	0.177	0.010	0.073	0.002	0.108	0.004	1.49	0.07
#3	−2.90	0.40	0.40	−5.50	0.80	0.80	0.10	0.24	0.165	0.005	0.100	0.005	0.058	0.002	0.032	0.003	0.55	0.05
#4	−3.30	0.42	0.42	−6.21	0.84	0.84	0.15	0.24	0.189	0.004	0.072	0.003	0.052	0.001	0.028	0.002	0.54	0.04
#5_outer left part[c]	−0.66	0.43	0.43	−1.20	0.85	0.85	0.01	0.24	0.151	0.005	0.117	0.005	0.071	0.003	0.078	0.007	1.10	0.11
#6	−3.79	0.45	0.45	−7.27	0.92	0.92	0.05	0.21	0.128	0.003	0.093	0.004	0.059	0.002	0.051	0.003	0.87	0.06
#7	−3.08	0.46	0.46	−5.85	0.93	0.93	0.05	0.21	0.142	0.003	0.163	0.005	0.073	0.002	0.093	0.003	1.28	0.05
Average (outer left) & 2SD	−0.54	0.34	0.34	−0.87	0.93	0.93	0.09	0.24	0.135	0.046	0.153	0.100	0.072	0.003	0.083	0.014	1.16	0.21
Average (#2−4 & #6–7) & 2SD	−3.28	0.67	0.67	−6.22	1.32	1.32	0.09	0.08	0.142	0.081	0.121	0.093	0.063	0.019	0.063	0.073	0.99	1.19
502																		
#1	−0.62	0.44	0.44	−1.16	0.85	0.85	−0.05	0.24	0.033	0.001	0.320	0.011	0.063	0.002	0.074	0.003	1.18	0.06
#2	−0.58	0.44	0.44	−0.87	0.85	0.85	0.14	0.24	0.045	0.002	0.316	0.010	0.078	0.004	0.084	0.004	1.08	0.08
#3	−0.59	0.41	0.41	−0.92	0.77	0.77	0.13	0.24	0.037	0.002	0.321	0.011	0.075	0.002	0.314	0.015	4.20	0.23
#4	−0.50	0.40	0.40	−0.90	0.77	0.77	−0.03	0.24	0.037	0.001	0.295	0.010	0.072	0.002	0.283	0.002	3.92	0.10
Average & 2SD	−0.57	0.11	0.11	−0.96	0.26	0.26	0.05	0.21	0.038	0.010	0.313	0.017	0.072	0.013	0.189	0.255	2.62	3.57
503																		
#1	−1.72	0.45	0.45	−3.34	0.93	0.93	−0.07	0.21	0.039	0.001	0.212	0.008	0.062	0.003	0.088	0.002	1.42	0.07
#2	−1.85	0.44	0.44	−3.48	0.91	0.91	0.06	0.21	0.063	0.001	0.164	0.006	0.061	0.002	0.024	0.002	0.40	0.04
#3	−2.06	0.46	0.46	−3.87	0.94	0.94	0.05	0.21	0.052	0.003	0.195	0.008	0.063	0.002	0.042	0.002	0.67	0.05
#4	−2.26	0.47	0.47	−4.24	0.94	0.94	0.06	0.21	0.052	0.002	0.152	0.005	0.072	0.004	0.067	0.003	0.93	0.07
Average & 2SD	−1.97	0.48	0.48	−3.74	0.81	0.81	0.03	0.13	0.051	0.020	0.181	0.039	0.065	0.010	0.055	0.056	0.86	0.87

Table 4 (*continued*)

Sample/Location #[a]	$\delta^{25}Mg_{DSM-3}$ (‰)	Unc. (+/−) (2σ)		$\delta^{26}Mg_{DSM-3}$ (‰)	Unc. (+/−) (2σ)		$\delta^{26}Mg^*$ (‰)	Unc. (2σ)	CaO (wt%)	Unc. (2σ)	Cr_2O_3 (wt%)	Unc. (2σ)	FeO (wt%)	Unc. (2σ)	MnO (wt%)	Unc. (2σ)	MnO/FeO	Unc. (2σ)
505																		
#1	−0.86	0.46	0.46	−1.51	0.94	0.94	0.08	0.21	0.060	0.001	0.259	0.010	0.080	0.004	0.135	0.006	1.70	0.11
#2	−0.68	0.40	0.40	−1.18	0.84	0.84	0.13	0.21	0.079	0.003	0.128	0.004	0.058	0.003	0.026	0.002	0.45	0.05
#3	−1.17	0.42	0.42	−2.30	0.88	0.88	−0.06	0.21	0.066	0.002	0.179	0.006	0.062	0.002	0.073	0.002	1.18	0.05
#4	−1.06	0.41	0.41	−2.15	0.86	0.86	−0.10	0.21	0.075	0.003	0.129	0.004	0.057	0.002	0.019	0.002	0.33	0.03
Average & 2SD	−0.94	0.44	0.44	−1.79	1.05	1.05	0.02	0.22	0.070	0.017	0.174	0.087	0.064	0.021	0.063	0.108	0.99	1.71
511																		
#1	−2.36	0.44	0.44	−4.49	0.86	0.86	0.08	0.25	0.090	0.002	0.096	0.006	0.046	0.003	0.020	0.003	0.44	0.06
#2	−2.91	0.48	0.48	−5.57	0.92	0.92	0.00	0.25	0.077	0.002	0.123	0.005	0.044	0.003	0.090	0.005	2.02	0.16
#3	−2.52	0.43	0.43	−5.02	0.85	0.85	−0.15	0.25	0.101	0.002	0.128	0.007	0.044	0.001	0.095	0.002	2.14	0.08
#4	−3.34	0.46	0.46	−6.41	0.89	0.89	0.03	0.25	0.109	0.005	0.113	0.007	0.056	0.003	0.005	0.001	0.09	0.01
Average & 2SD	−2.78	0.87	0.87	−5.37	1.64	1.64	−0.01	0.20	0.094	0.027	0.115	0.020	0.048	0.011	0.052	0.093	1.10	1.97
512																		
#1	−1.09	0.47	0.47	−1.96	0.94	0.94	0.05	0.21	0.040	0.001	0.273	0.009	0.068	0.002	0.215	0.003	3.18	0.10
#2	−1.10	0.47	0.47	−1.97	0.94	0.94	0.06	0.21	0.037	0.001	0.233	0.008	0.068	0.002	0.088	0.002	1.28	0.05
#3	−1.25	0.46	0.46	−2.30	0.92	0.92	0.03	0.21	0.032	0.001	0.245	0.008	0.066	0.002	0.048	0.002	0.73	0.04
Average & 2SD	−1.15	0.18	0.18	−2.08	0.38	0.38	0.05	0.04	0.036	0.008	0.250	0.029	0.067	0.003	0.117	0.174	1.74	2.59
513																		
#1	−0.47	0.42	0.42	−0.78	0.82	0.82	0.13	0.25	0.269	0.006	0.055	0.003	0.042	0.003	0.0039	0.0009	0.09	0.02
#2	−0.83	0.45	0.45	−1.44	0.87	0.87	0.12	0.25	0.249	0.006	0.062	0.004	0.032	0.001	0.0046	0.0011	0.14	0.03
#3	−0.57	0.44	0.44	−1.02	0.86	0.86	0.06	0.25	0.283	0.007	0.078	0.004	0.039	0.001	0.0040	0.0005	0.10	0.01
Average & 2SD	−0.62	0.37	0.37	−1.08	0.67	0.67	0.10	0.08	0.267	0.035	0.065	0.017	0.038	0.010	0.004	0.001	0.11	0.04

[a] Analysis points are shown in Electronic Annex EA3.

[b] Average values are listed for minor element data. Individual data are reported in Electronic Annex EA4-3-3.

[c] These data are obtained from an outer left part of AOA 501, which shows compact textures relative to the most part of this AOA.
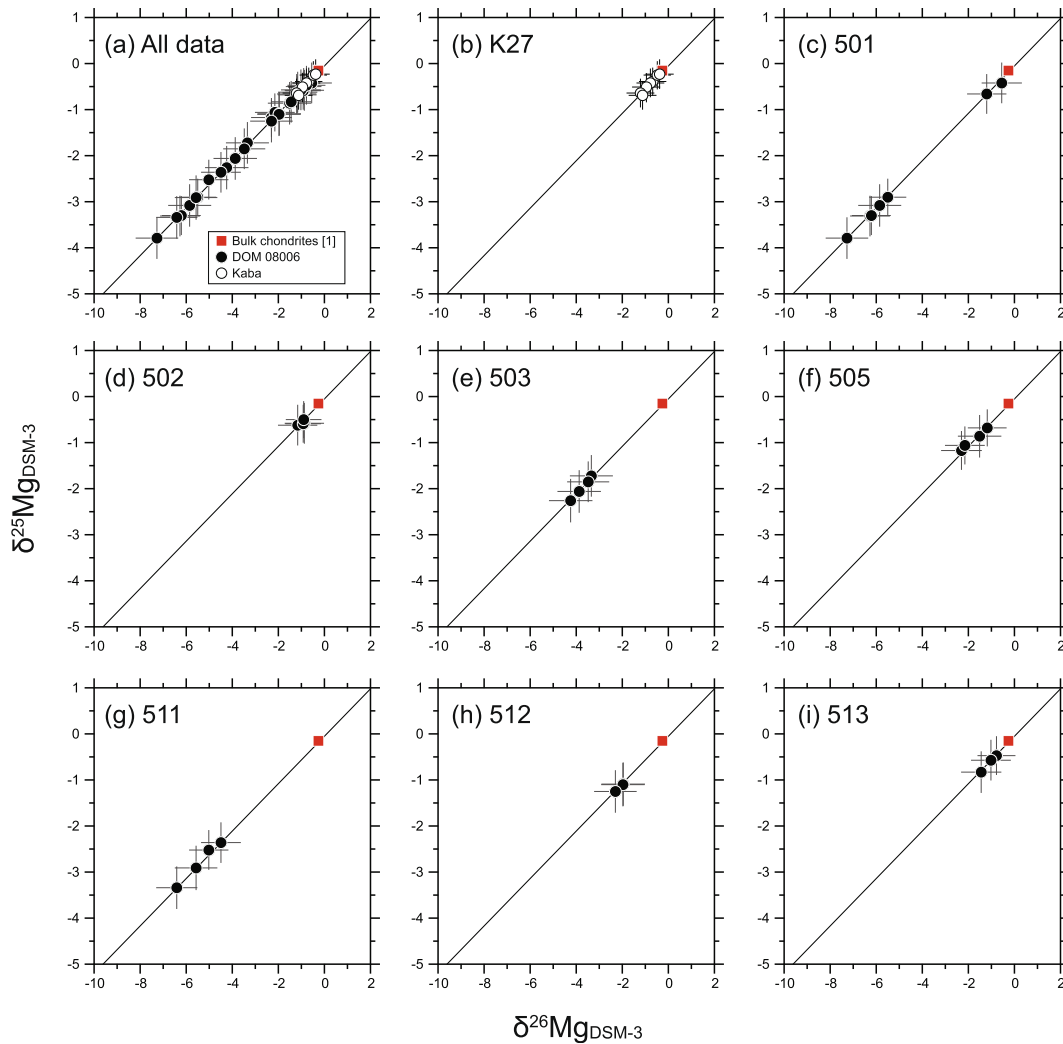
Fig. 7. Magnesium-three isotope ratios of the eight AOA olivines from Kaba and DOM 08006. All measured data are shown in (a). (b–i) Individual AOA diagrams from Kaba (b) and DOM 08006 (c–i). Square symbols represent the Mg isotope ratios of bulk chondrites ([1] Teng et al., 2010). Solid lines represent a best-fit line for all the measured data determined by a least squares fitting (Ludwig, 2012). Errors are 2σ.

(δ^{25}Mg = –0.15 ± 0.04‰, δ^{26}Mg = –0.28 ± 0.07‰, 2SD). In this study, the Mg isotope regression for AOA olivines is δ^{25}Mg′ = (–0.06 ± 0.04) + (0.516 ± 0.012) × δ^{26}Mg′ (Fig. 8). If using the δ^{26}Mg′ value of bulk chondrites (Teng et al., 2010) in this formula, the calculated δ^{25}Mg′ is –0.20 ± 0.04‰ (95% confidence limit), which is indistinguishable from that of the bulk chondrites within their uncertainties. This suggests that AOA olivines originated from a reservoir with a chondritic Mg isotope ratio.

Five Wild 2 particles show resolvable variability in Mg isotope ratios (Fig. 9). All Wild 2 olivine analyses fall on a mass-dependent fractionation line defined by individual AOA analyses (Fig. 9), suggesting Wild 2 olivine particles also derived from a chondritic Mg isotope reservoir. While uncertainties from comet particles are relatively larger, our data demonstrate for the first time that Mg isotopes are in agreement between Wild 2 comet olivine particles and other known Solar System solids.

5.3. Origin of AOAs: Condensation and thermal processing in the solar protoplanetary disk

5.3.1. Variations in texture among AOAs

Earlier studies have hypothesized a condensation origin for AOAs based on textural and mineralogical signatures (Krot et al., 2004a and references therein). The porous and irregular shapes of some AOAs indicate that they are aggregates of olivine grains and were never completely molten (e.g., Grossman and Steele, 1976; Krot et al., 2004a and references therein). Also, the presence of silica in an AOA from the Yamato-793261 (CR) is indicative of gas–solid condensation (Komatsu et al., 2018). The AOAs studied here show textural variations (Figs. 3–5), allowing for interpreting their origins. Three of them (K27, 505 and 513) have a compact texture with little porosity in their forsterite portions (Fig. 3), similar to "compact AOAs" from Yamato-81020 (CO3.05) (Sugiura et al., 2009). In contrast,
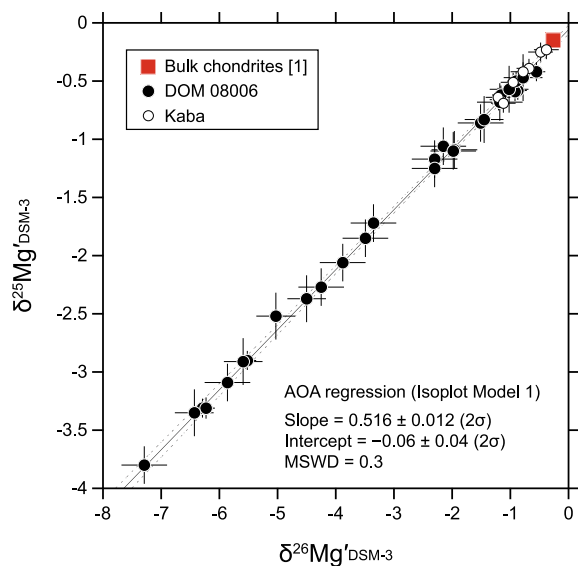
Fig. 8. Relationships between $\delta^{25}Mg'_{DSM-3}$ and $\delta^{26}Mg'_{DSM-3}$ values of individual AOA olivine analyses. The square symbol represents the Mg isotope ratios of bulk chondrites ([1] Teng et al., 2010). The solid line represents a linear regression line (Isoplot model 1; Ludwig, 2012) for all AOA data (N = 36) obtained in this study. The dotted curves are error envelopes that show 95% confidence limits. Note that uncertainties of $\delta^{25}Mg'_{DSM-3}$ and $\delta^{26}Mg'_{DSM-3}$ values were not propagated from those related to instrumental mass fractionation. See more details in Electronic Annex EA5.

AOAs 502 and 503 are porous, irregularly shaped objects (Fig. 4), similar to "porous AOAs" reported in Sugiura et al. (2009). Compact and porous AOAs are found in other types of carbonaceous chondrites (e.g., Krot et al., 2004a, 2014; Weisberg et al., 2004; Ruzicka et al., 2012; Rubin, 2013; Han and Brearley, 2015; Komatsu et al., 2015), suggesting this textural variation is a general characteristic among AOAs. From our observations, we categorize the nine AOAs investigated here into two types of AOAs; (1) three AOAs, K27, 505, and 513 are categorized as compact AOAs, as they have almost no pores and show a concentric texture with spinel and/or anorthite at the core → Al-diopside → forsterite (Fig. 3c, e, g); and (2) those with pore-rich, irregular-shaped, ±fine-grained textures are categorized as pore-rich AOAs (501, 502, 503, 511, 512, 514; Figs. 4 and 5). Spinel grains are observed in compact AOAs, but are not present in pore-rich AOAs of this study. Conversely, diffuse Ca-Al-rich haloes are observed in pore-rich AOAs, but are not a feature of compact AOAs. Moreover, the pores within pore-rich AOAs have polygonal outlines (e.g., Fig. 4b–d and f–g), suggesting these AOAs avoided melting (Han and Brearley, 2015).

Many AOAs do not appear to be the result of simple condensation (e.g., Komatsu et al., 2009, 2015). As shown in Fig. 3, compact AOA olivines have low porosity textures, indicating that they experienced high-temperature annealing after their condensation and aggregation (e.g., Krot et al., 2004a; Sugiura et al., 2009; Komatsu et al., 2009; Han and Brearley, 2015). In addition, compact AOAs

K27 and 513 contain 5–10 μm size anorthite that is rimmed by 5–10 μm thick Al-diopside, which is in turn rimmed by olivine grains (Fig. 3c and e). This texture is not consistent with a sequence that is predicted by equilibrium condensation calculations (Petaev and Wood, 2005). Komatsu et al. (2009) performed heating experiments on mineral assemblages similar to those of AOAs and suggested that Al-diopside in AOAs can be produced from a small degree of melting of forsterite and anorthite. Based on the compact texture and the occurrence of Al-diopside between forsterite and anorthite (Fig. 3c and e), it appears that some AOAs experienced high-temperature annealing.

Similar occurrences of Al-diopside between forsterite and anorthite are also found among pore-rich AOAs (e.g., Fig. 5b and c), but at much finer scales. In addition, minor low-Ca pyroxenes are found in two pore-rich AOAs (502 and 503), which occur with Fe,Ni-metal (Fig. 4b, d, g). Similar textural occurrences of low-Ca pyroxene are present in AOAs from CR chondrites (Krot et al., 2004b). The existence of low-Ca pyroxene suggests interaction with gaseous SiO or direct condensation (Krot et al., 2004b). These observations indicate that some pore-rich AOAs have also experienced high-temperature annealing, although to a smaller degree relative to compact AOAs.

5.3.2. Variations in minor element abundances among AOAs

Among the AOAs investigated there is an inconsistency in FeO contents determined by EPMA versus SIMS (Fig. 11). Previous studies employing EPMA found that AOA olivines from the least metamorphosed chondrites have detectable FeO (~1 wt%; e.g., Krot et al., 2004a; Weisberg et al., 2004; Itoh et al., 2007; Sugiura et al., 2009; Komatsu et al., 2015, 2018), most of which are more enriched than concentrations predicted by equilibrium condensation calculations (e.g., ~0.14 wt% at a total pressure of 10^{-4} bar and with a dust enrichment factor of 1 (nominal solar composition); Sugiura et al., 2009). The enrichment in FeO suggests condensation of olivine at more oxidizing conditions (=high dust/gas ratios) (e.g., Komatsu et al., 2015, 2018). Our FE-EPMA-derived FeO contents from AOA olivines are variable (~0.05–1 wt%; open symbols in Fig. 11), with some values that are also much higher than that predicted by Sugiura et al. (2009). In contrast, our SIMS data reveal uniform olivine FeO contents of ~0.05 wt% among the AOAs studied (with a few exceptions for Kaba AOA K27; Fig. 11), which is consistent with equilibrium condensation calculations with a nominal solar composition gas from Sugiura et al. (2009). The uniform olivine FeO contents suggest that AOA olivine formed at more reducing conditions than previously thought. As higher FeO is mostly observed in porous AOAs, Sugiura et al. (2009) pointed out the possibility of contributions from FeO-bearing matrix materials during olivine EPMA analyses. Our present results also indicate that FeO contents of AOA olivine determined by EPMA analyses tend to be influenced by fluorescence from surrounding matrix materials and/or Fe,Ni-metals in AOAs, and that this may result in an overestimation of FeO contents and in an underestimation of MnO/FeO ratios in AOA olivine. The similar problem on EPMA analyses has also been

Table 5
Magnesium isotope ratios and minor elemental abundances of Wild 2 olivine particles obtained with SIMS.

Sample/Location #[a]	$\delta^{25}Mg_{DSM-3}$ (‰)	Unc. (+/−) (2σ)		$\delta^{26}Mg_{DSM-3}$ (‰)	Unc. (+/−) (2σ)		$\delta^{26}Mg^*$ (‰)	Unc. (2σ)	CaO (wt%)	Unc. (2σ)	Cr_2O_3 (wt%)	Unc. (2σ)	FeO (wt%)	Unc. (2σ)	MnO (wt%)	Unc. (2σ)	MnO/FeO	Unc. (2σ)
^{16}O-depleted particles																		
T77/F4																		
#1	−0.17	0.77	0.51	−0.46	1.17	0.87	−0.07	0.43	0.186	0.015	0.07	0.01	29.72	0.99	0.481	0.005	0.016	0.001
T149/F1																		
#1	−0.53	0.70	0.70	−0.74	1.05	1.05	−0.06	0.76	0.115	0.009	0.51	0.05	12.24	0.41	0.332	0.008	0.027	0.001
#2	−0.40	0.70	0.70	−0.78	1.05	1.05	−0.33	0.76	0.116	0.009	0.53	0.06	12.84	0.43	0.342	0.008	0.027	0.001
#3	−0.36	0.70	0.70	−0.77	1.05	1.05	−0.41	0.76	–	–	–	–	–	–	–	–	–	–
#4	−0.70	0.70	0.70	−0.87	1.05	1.05	0.16	0.76	–	–	–	–	–	–	–	–	–	–
Average & 2SD	−0.50	0.30	0.30	−0.79	0.11	0.11	−0.16	0.52	0.116	0.001	0.52	0.03	12.54	0.85	0.337	0.014	0.027	0.002
^{16}O-rich particles																		
T57/F10																		
#1	0.56	0.47	0.63	1.40	0.97	1.30	0.15	0.45	0.043	0.003	0.42	0.05	1.75	0.06	0.664	0.016	0.38	0.02
T77/F50																		
#1	−0.97	0.41	0.49	−1.68	0.76	1.01	0.08	0.71	–	–	–	–	–	–	–	–	–	–
#2	−0.93	0.41	0.49	−1.69	0.76	1.01	−0.01	0.70	0.031	0.002	0.31	0.03	0.065	0.003	0.247	0.004	3.80	0.16
#3	−0.60	0.41	0.49	−0.94	0.76	1.01	0.11	0.70	–	–	–	–	–	–	–	–	–	–
Average & 2SD	−0.83	0.40	0.40	−1.44	0.87	0.87	0.06	0.13										
T175/F1																		
#1	−0.48	0.51	0.62	−0.47	1.04	1.26	0.31	0.37	0.0038	0.0003	0.15	0.02	0.151	0.015	0.055	0.004	0.37	0.05

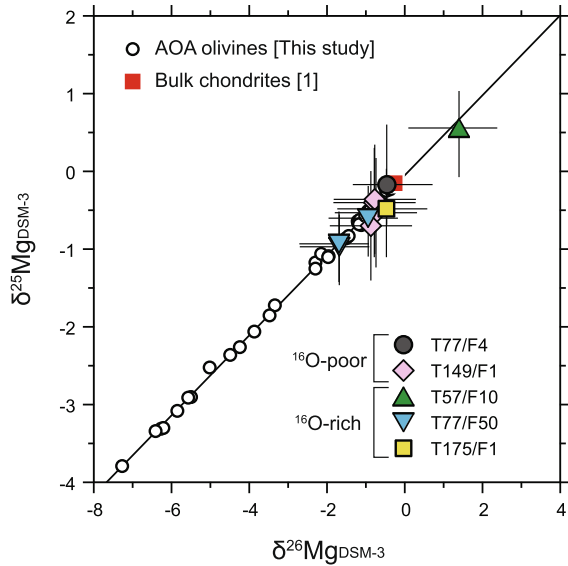[a] Analysis points are shown in Electronic Annex EA1.

Fig. 9. Magnesium-three isotope ratios of the five Wild 2 olivine particles studied. The red square symbol represents the Mg isotope ratios of bulk chondrites ([1] Teng et al., 2010). All measured AOA data (Fig. 7a) are shown for comparison. Errors for Wild 2 olivine data are 2σ. For clarity, errors for AOA data are not shown. (For interpretation of the references to color in this figure legend, the reader is referred to the web version of this article.)
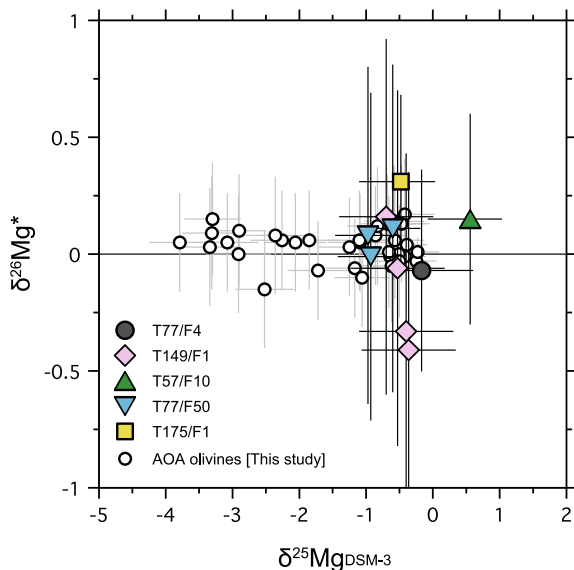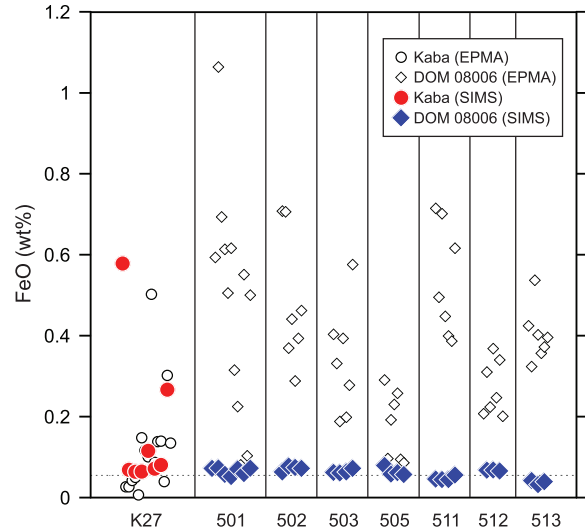

Fig. 11. FeO contents (wt%) of AOA olivines from Kaba and DOM 08006. Data obtained with FE-EPMA (open symbols) and SIMS (closed symbols) are shown. Data obtained with FE-EPMA might be overestimated due to secondary fluorescence effects (see Section 5.3.2). The dotted line represents the detection limit (0.05 wt%) for FE-EPMA analyses.

Fig. 10. $\delta^{26}Mg^*$-$\delta^{25}Mg_{DSM-3}$ plot for AOA olivines (Kaba and DOM 08006) and the five Wild 2 olivine particles studied.

minor element abundances, including FeO contents, obtained by SIMS in the following discussion.

In Fig. 12 CrO and MnO contents from SIMS olivine analyses are plotted as functions of CaO (Fig. 12a and b) and FeO (Fig. 12c and d), along with predicted values from Sugiura et al. (2009). Here we use CrO contents instead of Cr_2O_3 to compare SIMS data and predicted values from Sugiura et al. (2009). Generally, CrO (and possibly MnO) contents of AOA olivine are anti-correlated with CaO contents (Fig. 12a and b). Some olivines in pore-rich AOAs are enriched in Cr and Mn and are depleted in Ca relative to those in compact AOAs, but ~70% plot within a narrow range (CaO ~ 0.05–0.2 wt%; Fig. 12a and b). The correlations between textures and volatility controlled elemental abundances of AOAs are consistent with observations from Sugiura et al. (2009) and Komatsu et al. (2015), and indicate that compact AOAs are more refractory than pore-rich AOAs. As shown in Fig. 12c and d, plots of MnO and CrO versus FeO contents in AOA olivine are similar to those predicted by condensation models with a dust enrichment factor of 1 (nominal solar composition), except for some Kaba K27 AOA data. While all DOM 08006 data show a limited range in FeO contents regardless of their textural variations (compact versus pore-rich), it is possible that some Kaba AOA olivines were influenced by parent body alteration, leading to subtle Fe addition. Using data from DOM 08006 alone, we find CrO, MnO, and FeO compositions of AOA olivine are slightly offset, but broadly consistent with the condensation paths calculated by Sugiura et al. (2009) (Fig. 12c and d). In contrast, when CrO and MnO are plotted against CaO (Fig. 12a and b), they are clearly offset from the condensation paths, which is similar to AOA data reported in Sugiura et al. (2009). These relationships could be the result of two possibilities:
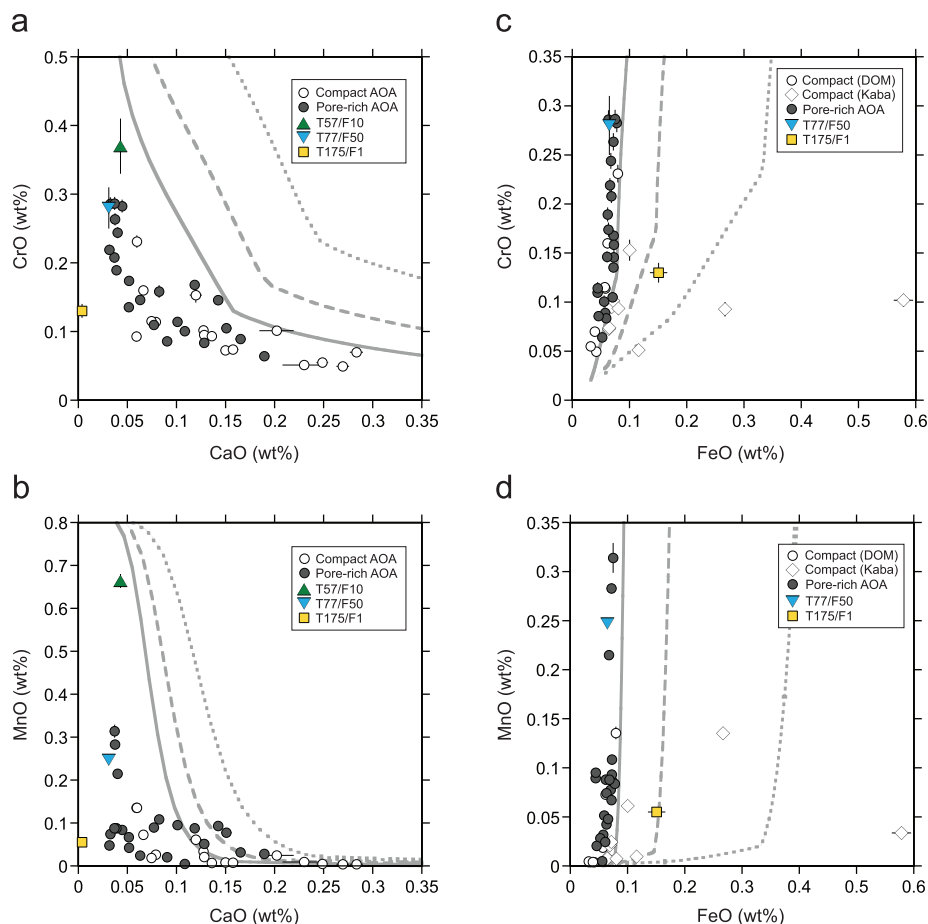
pointed out by Wasson et al. (1994), who demonstrated that FeO contents in enstatite grains separated from EL6 meteorite chips are an order of magnitude lower than those in meteorite thin sections, suggesting a secondary fluorescence and/or double backscattering of electrons from surrounding opaque minerals. Therefore, we only refer to

Fig. 12. Minor element systematics of ^{16}O-rich Wild 2 olivine particles (T57/F10, T77/F50, and T175/F1) and AOA olivines from Kaba and DOM 08006 obtained by SIMS. (a and c) CrO contents as functions of (a) CaO and (c) FeO. (b and d) MnO contents as functions of (b) CaO and (d) FeO. Equilibrium condensation trajectories at 10^{-4} bar with dust enrichment factor = 1 (nominal solar composition shown by solid curve), 2 (dashed curve), and 5 (dotted curve) calculated by Sugiura et al. (2009) are shown for comparison. Data for T57/F10 are not shown in (c) and (d) because of its high FeO content (1.75 wt%).

(1) equilibrium condensation with lower dust/gas ratios (dust enrichment factor < 1), or (2) disequilibrium condensation of AOA olivine. In the case of (1), the condensation paths in Fig. 12c and d could be shifted to a lower side with respect to FeO contents (X-axis) because disk environments with very low dust/gas ratios could have resulted in lower FeO contents of condensed olivine without significant changes in MnO and CrO contents (Sugiura et al., 2009; Komatsu et al., 2015). However, even in environments with lower dust/gas ratios, CaO contents in AOA olivine may not be significantly reduced when compared to those predicted from condensation calculations (Fig. 12a and b). In the case of (2), disequilibrium condensation could explain low concentrations of CaO relative to those predicted from a model condensation path. In the temperature range of equilibrium olivine condensation (e.g., 1300–1370 K at 10^{-4} bar with a dust enrichment factor of 1), most Ca is predicted to be consumed by the formation of Ca-Al-rich minerals that do not remain in the gas phase (Sugiura et al., 2009). Thus, if AOA olivine condensed from the gas phase and was never equilibrated with pre-existing Ca-Al-rich minerals, CaO contents in olivine would be lower than

those expected by equilibrium condensation. In contrast, Mn and Cr would have been largely in the gas phase, such that MnO and CrO abundances versus CaO contents in AOA olivine would plot parallel to the equilibrium condensation trajectories (Fig. 12a–d). Therefore, the observed offsets from condensation paths indicate that AOAs formed by disequilibrium condensation.

5.3.3. Kinetic isotope fractionation during condensation

During condensation, mineral phases can become enriched in light isotopes due to disequilibrium effects. For example, Richter (2004) modeled Mg isotope fractionation during condensation and demonstrated that Mg isotopes of the condensate are enriched in lighter isotopes when the ambient temperature changes faster than the condensation timescale. In this condition, the pressure of Mg gas is greater than its saturation vapor pressure, which facilitates disequilibrium condensation. This supersaturated condition could produce condensates enriched in lighter isotopes.

Fig. 13a shows δ^{25}Mg values for individual olivines from AOAs with different textures (compact versus pore-rich).

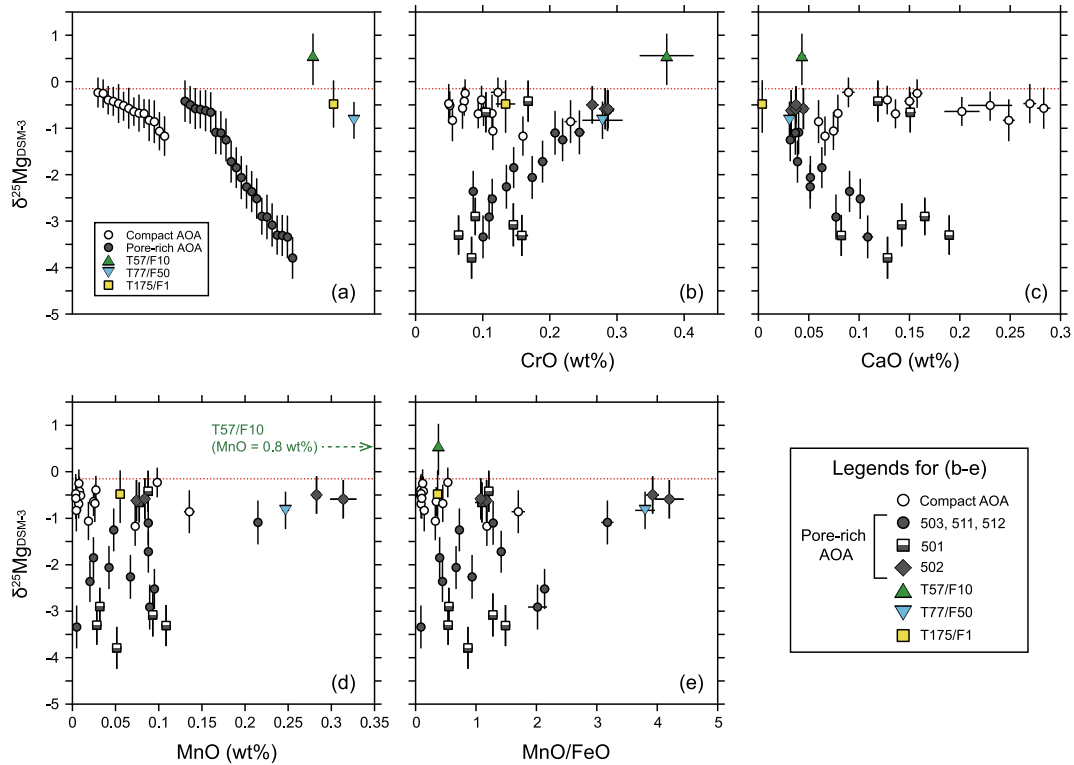Fig. 13. Relationships among Mg isotope ratios and minor element abundances of ^{16}O-rich Wild 2 olivine particles (T57/F10, T77/F50, and T175/F1) and AOA olivines from Kaba and DOM 08006 obtained by SIMS. Open circle symbols represent AOA olivines with compact textures (compact AOA), while closed circle, diamond, and half-closed square symbols represent AOA olivines with pore-rich textures (pore-rich AOA; see Section 5.3.1 for details). The dotted lines represent the Mg isotope ratio of bulk chondrites (Teng et al., 2010). (a) δ^{25}Mg$_{DSM-3}$ values of three ^{16}O-rich Wild 2 particles and AOA olivines with different textures (compact versus pore-rich). (b–e) δ^{25}Mg$_{DSM-3}$ values as functions of (b) CrO, (c) CaO, (d) MnO contents (wt%) and (e) MnO/FeO (wt%) ratio. Errors are 2σ.

Compact AOAs are more limited in δ^{25}Mg values (–1.2‰ to chondritic), while pore-rich AOAs exhibit greater variability (–3.8‰ to chondritic). As pore-rich AOAs may have experienced limited post-formation annealing, their larger and more negative δ^{25}Mg variations may have been caused by disequilibrium condensation processing. As discussed earlier, variations of trace element abundances in AOA olivine suggest they are controlled by volatility even though concentrations do not exactly follow equilibrium condensation trajectories. The δ^{25}Mg values in pore-rich AOA olivine correlate positively with CrO and negatively with CaO contents, respectively (Fig. 13b and c), which could represent a condensation trajectory in a cooling nebula gas.

A similar positive correlation between δ^{25}Mg and MnO concentration is expected, but is not clearly seen in Fig. 13d. Most AOAs have MnO contents <0.1 wt% and a large range of δ^{25}Mg. Equilibrium condensation calculations by Sugiura et al. (2009) predict that condensation of Mn into olivine should occur at a lower temperature than Cr, and that the increase of MnO with decreasing temperature is steeper than that of CrO (see Fig. 2 in Sugiura et al., 2009). If the cooling rate is faster than the equilibrium condensation timescale (i.e., disequilibrium condensation), and if the temperature is within the range of Mn condensation, Mn will not sufficiently condense into olivine. Thus, rela-

tively lower MnO contents are consistent with kinetic mass-dependent isotope fractionation of Mg, due to supersaturated conditions during condensation of olivine.

Isotope fractionation of condensing forsterite has been modeled as functions of the condensation temperature and timescale parameter ε by Richter (2004),

$$\varepsilon = \frac{\tau_{cond}}{\tau_T} = \frac{\lambda_T V_c \rho_i \eta^{-\frac{1}{3}}}{A J_{i,0}} \qquad (1)$$

where τ_{cond} and τ_T are timescales for condensation and for ambient temperature change, respectively, V_c is the volume of the condensed phase, ρ_i is the molar density of i in the condensed phase, A is the surface area, and $J_{i,0}$ is the free evaporation rate at a specified temperature and pressure. The timescale of τ_T is an inverse of the cooling rate $\lambda_T = -(1/T)dT/dt$. As expected by this relationship, when the cooling rate is much faster than the timescale for condensation (i.e., larger ε value), it induces disequilibrium condensation and large isotopic fractionation by partial condensation. As a first approximation, the condensation temperature of AOA olivine is estimated by comparing the CrO content and the equilibrium condensation calculations at a total pressure of 10^{-4} bar and a dust enrichment factor of 1 (Sugiura et al., 2009). Fig. 14 shows δ^{25}Mg values of AOA olivines as a function of the estimated
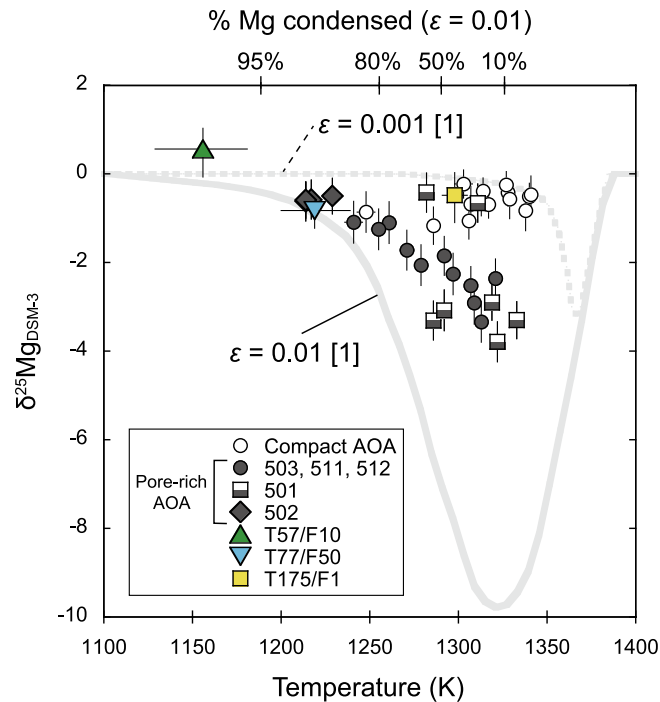
Fig. 14. $\delta^{25}Mg_{DSM-3}$ values as a function of estimated condensation temperatures for ^{16}O-rich Wild 2 olivine particles T57/F10, T77/F50, and T175/F1, and AOA olivines from Kaba and DOM 08006. Condensation trajectories of $\delta^{25}Mg$ as a function of condensation temperature and the timescale parameter ε modeled by Richter (2004) are shown for comparison (solid line with $\varepsilon = 0.01$ and dotted line with $\varepsilon = 0.001$). Fractions of magnesium condensed as forsterite with $\varepsilon = 0.01$ are also shown at the top of the plot. Condensation temperatures (X axis for each data point) are estimated by comparing CrO contents obtained by SIMS and an equilibrium condensation calculation at 10^{-4} bar with a dust enrichment factor of 1 (nominal solar composition) from Sugiura et al. (2009). Although negative Mg isotope fractionations suggest formation by disequilibrium condensation, we assume the CrO contents of olivine reflect their condensation temperatures (see Section 5.3.3 for more details). This assumption may result in additional uncertainties of estimated temperatures.

condensation temperatures, which are compared to the $\delta^{25}Mg$ trajectories during disequilibrium condensation modeled by Richter (2004). Since olivine crystallization would occur during disequilibrium condensation rather than during equilibrium condensation, the predicted temperatures are systematically higher than the actual temperatures depending on the extent of disequilibrium condensation. While there are uncertainties in our temperature estimates, pore-rich AOA olivine data are distributed between the two model disequilibrium condensation trajectories with $\varepsilon = 0.001$ and 0.01, respectively (Fig. 14). The negative correlation among most pore-rich AOA data (except for two AOA 501 analyses) are in agreement with a small range of ε, suggesting that variations in $\delta^{25}Mg$ values result from differences in the condensation temperature at a fairly constant cooling rate. Note that the isotopic fractionation calculations by Richter (2004) were done at a total pressure of 10^{-3} bar, which is one order of magnitude higher than that of the condensation calculation by Sugiura et al. (2009) that we use to estimate condensation temperatures. The total pressure influences the parameter $J_{i,0}$ in Eq. (1) (see Richter, 2004 for more details), and decreases it by a factor of 3 when the total pressure is lowered by 10^{-1} bar; in turn, this leads to increase ε by a factor of 3. Thus, it does not significantly affect our conclusion.

5.3.4. Effect of high-temperature annealing

If AOAs experienced high-temperature annealing in the solar nebula, Mg isotope signatures and correlated minor element concentrations that are seen in pore-rich AOA could have been modified from their primary values. At high temperatures, Cr could be lost and Mg isotope ratios could have exchanged with ambient gas (e.g., Solar $\delta^{25}Mg \sim 0$). Also, as a result of the presence of Ca-Al-rich phases in AOAs, Ca would likely have diffused into olivine (Sugiura et al., 2009). Such processes could have modified $\delta^{25}Mg$ values of AOA olivine, making them negatively correlated with CrO and positively correlated with CaO. However, this is not observed for the AOA data in this study (Fig. 13b-c). In particular, the diffusivity of Cr in forsterite varies with Cr concentration, oxygen fugacity, and silica activity (a_{SiO2}) (Jollands et al., 2018). At the onset of olivine condensation (1370 K at a total pressure of 10^{-4} bar and a dust enrichment factor of 1; Sugiura et al., 2009), the Cr diffusion rate in forsterite (along the c axis) ranges from 1×10^{-18} to 2×10^{-16} m^2/s (Jollands et al., 2018), which is faster than the Mg diffusion rate in forsterite (5×10^{-19} m^2/s; Chakraborty, 2010). Hence, high-temperature annealing would likely have resulted in the loss of Cr from olivine before Mg isotopes exchanged with ambient gas. Thus, the positive correlation between

δ^{25}Mg and CrO contents in pore-rich AOAs (Fig. 13b) suggest that high-temperature annealing did not significantly modify the Mg isotope and chemical signatures of pore-rich AOAs, a finding which is consistent with textural observations, such as irregular shapes of these AOAs. Additionally, Ca diffusion in forsterite is comparable with that of Mg (1×10^{-19} m^2/s at 1370 K along the c axis; Morioka, 1981; Coogan et al., 2005) meaning that the inverse relationship between δ^{25}Mg and CaO contents (Fig. 13c) also supports a conclusion that Mg isotope characteristics of pore-rich AOAs have not been modified by annealing.

As previously mentioned, a positive correlation between δ^{25}Mg and MnO contents (or MnO/FeO ratios) is not apparent (Fig. 13d and e), which is likely the result of disequilibrium condensation. Alternatively, high-temperature annealing could lead to a loss of Mn from olivine grains. If this is the case, MnO contents as well as MnO/FeO ratios of some AOAs might have been modified during the annealing. However, the Mn diffusion rate in forsterite, which is influenced by oxygen fugacity and silica activity, ranges from 3×10^{-20} to 1×10^{-17} m^2/s at 1370 K along the c axis (Jollands et al., 2016). This is similar to or slightly lower than the Mn-Mg inter-diffusion rate, which was determined by Morioka (1981) to be 4.2×10^{-17} m^2/s at 1370 K along the c axis. Therefore, low MnO contents of pore-rich AOAs might not be caused by loss of Mn during high-temperature annealing.

5.3.5. Formation of compact AOAs

As mentioned above, δ^{25}Mg values of compact AOAs are nearly uniform (Fig. 13a), indicating partial isotope exchange with ambient gas during high-temperature annealing. Sugiura et al. (2009) proposed that compact AOA textures resulted from either annealing of pre-existing AOAs in the solar nebula or by slow cooling during condensation. Both hypotheses are consistent with the δ^{25}Mg uniformity in compact AOAs. If the former is the case, the duration of annealing would likely have been much longer than that for pore-rich AOAs, and may have induced Mg isotope exchange between AOA olivine and ambient gas. If the latter is the case, the cooling rate of compact AOAs would have been sufficiently slower than that of pore-rich AOAs (i.e., smaller ε value). Such slow cooling could achieve near-equilibrium condensation, which would suppress isotopic fractionation during condensation (e.g., dotted line, Fig. 14). This scenario is also consistent with the observed uniformity in compact AOA olivine δ^{25}Mg (Fig. 14). However, as discussed above, the mineralogical sequence observed in compact AOAs is inconsistent with an equilibrium condensation sequence (Petaev and Wood, 2005; Komatsu et al., 2009). In addition, minor element systematics in AOA olivines cannot be simply explained by equilibrium condensation (e.g., Fig. 12a). Therefore, long-term, high-temperature annealing of pre-existing AOAs appear to be the most likely scenario to explain the chemical, textural, and Mg isotopic signatures among compact AOAs, consistent with the conclusion of previous studies (e.g., Komatsu et al., 2001; Krot et al., 2004a; Han and Brearley, 2015; Marrocchi et al.,

2019a). Regarding O isotope ratios, we do not find a resolvable difference between compact and pore-rich AOAs (Fig. 6b), suggesting that (1) the annealing process did not modify the O isotope ratios because of its slower diffusion rate than Mg (Ando et al., 1981), and/or (2) the annealing process occurred at ^{16}O-rich environments similar to where pore-rich AOAs condensed.

One pore-rich AOA, 501 from DOM 08006, exhibits a bimodal distribution on a Mg three-isotope plot (Fig. 7c). The irregularly shaped Ca-Al-rich portions and abundant pores (Fig. 5b) indicate that the majority of this AOA has not experienced extensive annealing like compact AOAs. However, two Mg isotope analyses for AOA 501 do not follow the condensation trend observed in pore-rich AOAs (Fig. 13b and c), making it difficult to explain the δ^{25}Mg variation in AOA 501 by a simple condensation process. The near-chondritic δ^{25}Mg values are found only in the outer left portion of the AOA, which has a compact texture (SIMS pits #1 and #5 in Fig. 5c) compared to rest of the AOA (Fig. 5b). Thus, it is possible that Mg isotope ratios of the compact textured region exchanged with ambient gas during annealing. Porous and compact textures have also been found in a single AOA from Adelaide (ungrouped C), which does not show evidence for melting (AOA #34b; Krot et al., 2004b). This AOA mainly consists of porous forsterite regions with very fine-grained anorthite and Al-diopside, and these domains are surrounded by compact forsterite rims (see Fig. 4d in Krot et al., 2004b). As shown in Fig. 5c, Ca-Al-rich phases in the outer left part of the AOA 501 are concentrated centrally in this region, similar to nodules in compact AOA K27 (Fig. 3b). Note that, however, an analysis of the outer right portion of the AOA (location #7 in Electronic Annex EA3) reveals a negative Mg isotope ratio (δ^{25}Mg = –3.1 ± 0.4‰; 2σ), meaning there is no systematic relationship between analysis locations and δ^{25}Mg values in AOA 501. Furthermore, CrO contents of inner and outer regions are similar to each other. Since Cr diffusion rate in forsterite is faster than the Mg diffusion rate in forsterite, the similar CrO contents in both inner and outer regions may not support the Mg isotope exchange with ambient gas during annealing. Similarly, we did not observe notable differences in minor element abundances and oxygen isotope ratios among AOA 501 (Table 3 and 4).

Recently, Marrocchi et al. (2019a) conducted SIMS oxygen, magnesium, and silicon isotope analyses of AOA olivine from Kaba (CV3.1), NWA 5958 (ungrouped C2, CM-like), and MIL 07342 (CO3.0–3.2) and found large negative Si isotope fractionations in AOA olivine (down to –5‰/amu). In contrast, Mg isotope ratios of these AOA olivines are near-chondritic to positively fractionated ($\sim$2‰ in δ^{25}Mg). Based on a model involving the condensation of olivine, they concluded that AOA olivines formed by rapid condensation ($\sim$days to weeks) followed by Mg isotope homogenization during thermal annealing that did not affect primary Si isotope ratios, due to much lower diffusion rates of Si than Mg (Chakraborty, 2010). The textures of these AOAs indicate they are similar to compact AOAs in our study and their near-chondritic Mg isotope data are also generally consistent with this study. However, most δ^{25}Mg values reported in Marrocchi et al. (2019a) are

slightly positively fractionated from the chondritic Mg isotopic compositions, which is not observed in this work, indicating that some AOAs experienced partial evaporative loss of Mg during annealing. Alternatively, this difference between datasets could be the result of complex matrix effects for SIMS Mg isotope analyses of olivine (Fukuda et al., 2020). Marrocchi et al. (2019a) also mentioned "complex" matrix effects on Mg isotope analyses, though they did not use the correction scheme employed here. Our preliminary results, that are calibrated using only Fo contents, also show slight positive δ^{25}Mg values of some AOA olivines (Fukuda et al., 2019a), similar to the results from Marrocchi et al. (2019a). Therefore, a component of the observed positive fractionations in AOA olivine from Marrocchi et al. (2019a) could be due to inaccurate corrections of SIMS matrix effects. For example, when we apply our new calibration method, that combines Fo contents and Mg^+/Si^+ ratios, δ^{25}Mg values do not show positive values, but instead range from –4‰ to bulk chondritic Mg isotope ratios (Fig. 7). These δ^{25}Mg values are in good agreement with δ^{29}Si values of AOA olivine (–5‰ < δ^{29}Si < 0‰) determined by Marrocchi et al. (2019a). This comparison is significant because similar δ^{25}Mg and δ^{29}Si values are predicted from theoretical calculations of isotope fractionation during disequilibrium condensation of olivine (Marrocchi et al., 2019a), supporting our conclusion that the pore-rich AOAs studied here preserved their primary condensation Mg isotopic fractionation characteristics.

5.4. Origin of ^{16}O-rich Wild 2 olivine particles

Three Wild 2 particles studied here, T57/F10, T77/F50, and T175/F1, are forsteritic olivines (>Fo$_{98}$) with ^{16}O-rich signatures (Nakashima et al., 2012; Defouilloy et al., 2017; Chaumard et al., 2018). TEM-EDX analyses revealed that one of the particles, T77/F50 is LIME olivine (Fo$_{99.8}$; Joswiak et al., 2012), which was confirmed by our SIMS-derived MnO/FeO (wt%) ratio of this particle (3.8 ± 0.2; 2σ). Magnesium isotope data from T77/F50 are negatively fractionated (δ^{25}Mg = –0.8 ± 0.4‰, δ^{26}Mg = –1.4 ± 0.9‰, 2SD; average values) relative to a chondritic composition. These values are similar to negative Mg isotope fractionations observed in some AOAs (Fig. 9), suggesting that the T77/F50 particle is linked to AOA olivines. In addition, minor element systematics of T77/F50 and their relationship with δ^{25}Mg are similar to those of pore-rich AOAs (Figs. 12a–d and 13b–e, respectively). In particular, the δ^{25}Mg and minor element values of T77/F50 cannot be distinguished from those of AOA 502, which is the most porous example studied here (Fig. 4a–d). Furthermore, the Δ^{17}O value of T77/F50 (–23.9 ± 1.6‰, 2SD; Nakashima et al., 2012), is identical to that of AOA 502 (Δ^{17}O = –24.2 ± 0.8‰, 2SD) within uncertainties. Thus, the chemical and isotopic agreement between T77/F50 and at least one pore-rich AOA indicates that T77/F50 likely formed by disequilibrium condensation from the solar nebula, within an AOA-forming region providing strong evidence for some materials in comet Wild 2 and chondrites to be sourced from similar nebular regions.

T175/F1 is also a nearly pure forsterite particle (Fo$_{99.8}$) with a Δ^{17}O value of –23.3 ± 1.4‰ (2SD; Chaumard et al., 2018). However, unlike T77/F50, T175/F1 is not negatively fractionated in its Mg isotopes, beyond analytical uncertainties. On plots comparing δ^{25}Mg-CrO-MnO, T175/F1 falls within the range of compact AOAs (Fig. 13b and d–e), suggesting they are related. Note that, however, the CaO content of T175/F1 (38 ± 3 ppm; 2σ) is remarkably lower than those of AOAs (Fig. 13c). The FeO content of T175/F1 is slightly higher than AOAs from DOM 08006 and is more consistent with Kaba compact AOA K27 (Fig. 12c and d). The slight enrichment in FeO suggests that either (1) minor Fe addition occurred after initial formation, like Kaba AOA K27, or (2) T175/F1 condensed at a higher dust/gas ratio (dust enrichment factor > 1). In either case, it is difficult to explain the depletion of CaO compared to AOA olivines, meaning T175/F1 may have a different origin than AOA olivines and T77/F50. ^{16}O-rich, FeO-poor olivines are also found in chondrules as relict materials (e.g., Ushikubo et al., 2012; Marrocchi et al., 2019b), but their CaO contents are similar to those of AOAs (Marrocchi et al., 2019b), meaning a link between T175/F1 and relict olivine is unlikely. Matrix materials of chondrites also include ^{16}O-rich, FeO-poor olivines (e.g., Nagashima et al., 2015). The average Ca content of matrix olivine grains from the Kakangari meteorite is 0.13 ± 0.56 wt% (Nagashima et al., 2015), which is higher than that of T175/F1 by a factor of ~30, indicative of an origin that is different than that of T175/F1 olivine.

Frank et al. (2014) conducted minor element analyses of more than forty Wild 2 olivine particles by TEM-EDX. Of six aerogel tracks (T57, T61, T111, T112, T130, and T154) with forsteritic olivine (>Fo$_{95}$), four (T57, T61, T111, and T112) have CaO-poor olivine (<0.09 wt%). Among them, T61 terminal particles have low FeO (<0.10 wt%), MnO and Cr$_2$O$_3$ (<0.07 wt%), and CaO (<0.09 wt%), which are similar to concentrations observed in T175/F1. Frank et al. (2014) also conducted minor element analyses of olivines from various types of chondrites. Since forsteritic olivines with very low CaO are not found in chondrites, Frank et al. (2014) suggested a link between T61 terminal olivine particles and olivines from aubrites. If this is also the case for T175/F1, it implies highly reducing, ^{16}O-rich environments existed in the solar protoplanetary disk at the time of T175/F1 formation.

T57/F10 olivine also has ^{16}O-rich oxygen isotopic characteristics (Δ^{17}O = –22.0 ± 1.3‰, 2SD; Nakashima et al., 2012) with a slight enrichment in FeO (1.75 ± 0.06 wt%; 2σ) compared to the other two ^{16}O-rich Wild 2 and AOA olivines (~0.58 wt%) discussed above. This particle is not LIME olivine (MnO/FeO wt% = 0.38 ± 0.02; 2σ), though the MnO content is distinctively higher (MnO = 0.66 ± 0.02 wt%; 2σ) than those of the other two ^{16}O-rich Wild 2 and AOA olivines (Fig. 12b). The Cr$_2$O$_3$ content is also slightly higher (CrO = 0.42 ± 0.05 wt%; 2σ) than those of the other two ^{16}O-rich Wild 2 and AOA olivines. Hence, T57/F10 olivine is relatively enriched in the moderately to slightly refractory elements Mn, Cr, and Fe. We note that T57/F10 exhibits slightly positive δ^{25}Mg and ^{26}Mg values (δ^{25}Mg = 0.6 $^{+0.5}/_{-0.6}$‰, δ^{26}Mg = 1.4 $^{+1.0}/_{-1.3}$‰; 2σ) that

are not observed in AOA olivines (Fig. 9). Therefore, if T57/F10 olivine formed by condensation, it likely occurred under different conditions relative to those of AOA olivines studied here. For example, Komatsu et al. (2015) modeled equilibrium condensation under various dust/gas ratios (dust enrichment factor = ~ 0.1–100) and predict that FeO and MnO contents, as well as the MnO/FeO ratio of T57/F10 are explained by equilibrium condensation at a higher dust/gas ratio (dust enrichment factor = ~20), and at relatively lower temperatures (<1200 K). If we assume T57/F10 olivine formed by equilibrium condensation with a dust enrichment factor of ~20, most olivine (~90%) is predicted to have condensed at temperatures near 1500 K (Komatsu et al., 2015), meaning that the fraction of olivines condensed at lower temperatures (<1200 K) like T57/F10 would be very minor. In contrast, olivine grains with similar chemical compositions are commonly reported from Wild 2 particles, chondrite matrices (Frank et al., 2014), and IDPs (Klöck et al., 1989), indicative of their ubiquitous presence in the outer Solar System, which is inconsistent with the minor fraction predicted by equilibrium condensation calculation (Komatsu et al., 2015). Alternatively, a volatile-rich olivine like T57/F10 could have experienced a complex thermal history, involving re-equilibration with surrounding gas (Komatsu et al., 2015). Although oxygen isotope ratios of primary matrix minerals in chondrites are not well investigated due to their extremely small sizes (≤1 μm), Nagashima et al. (2015) reported ^{16}O-rich matrix olivine grains from the Kakangari meteorite. This suggests a link between T57/F10 and matrix olivine grains. Further studies that combined oxygen and magnesium isotope analyses, and minor element abundance measurements could provide important constraints on relationships between cometary and interplanetary dust particles, and fine-grained materials in chondrite matrices.

5.5. Origin of ^{16}O-depleted Wild 2 olivine particles

Olivine particles T77/F4 and T149/F1 are FeO-rich (Fo_{60} for T77/F4; Joswiak et al., 2012 and Fo_{85} for T149/F1; Defouilloy et al., 2017) and have ^{16}O-depleted oxygen isotopic signatures ($\Delta^{17}O = -1.5 \pm 1.2‰$ (2SD) for T77/F4; Nakashima et al., 2012 and $\Delta^{17}O = -1.7 \pm 1.5‰$ (2σ) for T149/F1; Defouilloy et al., 2017). $\delta^{25}Mg$ values of T77/F4 and T149/F1 are $-0.2 ^{+0.8}/_{-0.5}‰$ (2σ) and $-0.5 \pm 0.3‰$ (2SD; average value), respectively, both of which are near-chondritic values. As discussed earlier for ^{16}O-rich Wild 2 olivines, near-chondritic Mg isotope ratios can be explained by equilibrium condensation. However, FeO contents of T77/F4 and T149/F1 are too high compared to those expected by equilibrium condensation (e.g., Komatsu et al., 2015), meaning such an origin is unlikely. Alternatively, FeO-rich and ^{16}O-depleted oxygen isotopic signatures are well explained by formation at high dust/gas ratios (dust enrichment factor = ~2500) in the protoplanetary disk (Tenner et al., 2015). In addition, the Fo contents and oxygen isotope ratios of T77/F4 and T149/F1 olivines are similar to those of type II chondrule olivines from CR and CH chondrites, indicative of a possible genetic link (Nakashima et al., 2012; Defouilloy et al.,

2017). The $\delta^{25}Mg$ values of T77/F4 and T149/F1 are within the range of those of bulk chondrules (e.g., Bouvier et al., 2013; Van Kooten et al., 2016; Olsen et al., 2016; Chen et al., 2018), supporting a link between Wild 2 ^{16}O-depleted particles and type II chondrules in chondrites. Note that these high precision Mg stable isotope data are from bulk chondrule analyses, not from chondrule olivine themselves. Future high precision Mg isotope analyses of chondrule olivines will give an opportunity to discuss their relations with ^{16}O-depleted Wild 2 olivines.

5.6. Implications for dust transportation in the solar protoplanetary disk

Magnesium isotope and minor element analyses of Wild 2 olivine particles suggest they underwent a variety of nebular processing. For example, oxygen and magnesium isotopes, and chemical compositions of Wild 2 LIME olivine T77/F50 are in excellent agreement with those of pore-rich AOA olivines from the DOM 08006 (CO3.01) carbonaceous chondrite. The Mg isotope ratios of T77/F50 are negatively fractionated, indicating this particle formed by disequilibrium condensation from the solar nebula. Since characteristic nebular temperatures beyond 5 astronomical units (AU) should not exceed 200 K (e.g., Desch et al., 2018), the condensation of T77/F50 from comet-forming regions (~tens of AU) seems unlikely. Instead, it is more likely that T77/F50 condensed within the inner protoplanetary disk (<1 AU), as ambient temperatures would have exceeded 1000 K during early Solar System evolution (Desch et al., 2018). This would also explain the ^{16}O-rich signatures of some Wild 2 olivine particles, as measurements of solar wind infer the proto-Sun was ^{16}O-rich (McKeegan et al., 2011). Therefore, the presence of ^{16}O-rich "condensed" olivine in comet 81P/Wild 2 provides evidence for material transport from the inner part of the Solar System outward, to comet-forming regions.

Mechanisms for such transportation have been hypothesized by several studies (Ciesla, 2007; Nakamura et al., 2008; Hughes and Armitage, 2010; Nakashima et al., 2012; Joswiak et al., 2017), in order to explain the presence of ^{16}O-rich CAI-like materials in comet 81P/Wild 2 (McKeegan et al., 2006; Simon et al., 2008; Matzel et al., 2010). Al-Mg isotope analyses of two ^{16}O-rich CAI-like materials in comet 81P/Wild 2, Coki and Inti, indicate the absence of live ^{26}Al at the time of their formation (Ishii et al., 2010; Matzel et al., 2010), in which the $^{26}Al/^{27}Al$ upper limit of Coki was determined to be $<1 \times 10^{-5}$. The absence of live ^{26}Al at the time of ^{16}O-rich Wild 2 materials indicates that they formed either (1) very early (i.e., before injection and homogenization of ^{26}Al in the Solar System), or (2) late formation (>1.7 Myr after CAIs: Matzel et al., 2010) after the decay of ^{26}Al if using a canonical ($^{26}Al/^{27}Al)_0$ of 5.2×10^{-5} (Jacobsen et al., 2008; Larsen et al., 2011), and assuming a homogeneous distribution of ^{26}Al in the early Solar System. In the case of (1), transport was efficient enough to deliver the earliest formed materials to the outer Solar System, which is consistent with earliest formed CAIs to be transported into the outer part of the solar protoplanetary disk (Yang and Ciesla, 2012;

Fukuda et al., 2019b; Larsen et al., 2020). In the case of (2), no evidence of live ^{26}Al within ^{16}O-rich Wild 2 materials indicates, conversely, that transport was not efficient enough to deliver the earliest formed materials with the canonical $(^{26}$Al$/^{27}$Al$)_0$ values from inner (<1 AU) to the outer Solar System (∼30 AU). In either case, the presence of the AOA-like olivine (T77/F50) could place important constraints on the efficiency of such transportation processes as well as residence time of dust in the solar protoplanetary disk. Due to the absence of Al-rich phases (e.g., anorthite) associated with the ^{16}O-rich olivine particles studied here, we cannot constrain the initial abundances of ^{26}Al when T77/F50 formed. However, Al-Mg isotope analyses of AOAs from primitive chondrites suggest they formed around a time similar to the formation of CV3 CAIs $(^{26}$Al$/^{27}$Al ∼ 5 × 10^{-5}; Itoh et al., 2007; Sugiura and Krot, 2007; MacPherson et al., 2012; Ushikubo et al., 2017), except for some AOAs in CH chondrites, which could have recorded admixing of ^{26}Al in the earliest stage of the Solar System evolution and/or might have experienced thermal annealing by an impact-generated plume (Krot et al., 2014). On the basis of chemical and isotopic similarities between T77/F50 and AOA olivines from DOM 08006, T77/F50 may also have formed at the same time as CAIs and AOAs, suggesting that the efficiency of the transportation processes was sufficient to transport solid particles from the inner (<1 AU) to the outer Solar System (∼30 AU) at the earliest stage of the Solar System evolution. Recently, Neveu and Vernazza (2019) conducted thermal evolution simulations for IDP-like bodies including D-type asteroids that may have formed within comet-forming regions (Fujiya et al., 2019), and predicted accretion of IDP-like bodies at least 5–6 Myr after the formation of CAIs in CV3 chondrites. If true, the presence of AOA-like olivine in the comet 81P/Wild 2 would indicate that the residence time of dust particles exceeded 5–6 Myr during the earliest stages of the Solar System evolution.

6. CONCLUSIONS

Magnesium isotope ratios and minor element abundances of ^{16}O-rich and ^{16}O-depleted Wild 2 olivine particles were investigated by SIMS. Oxygen and Mg isotope ratios and minor element abundances of AOA olivines from Kaba and DOM 08006 carbonaceous chondrites were also determined in order to compare with those of ^{16}O-rich Wild 2 olivine particles.

Oxygen isotope data from Kaba and DOM 08006 AOA olivine are identical within uncertainties; they are also in agreement with oxygen isotope data from Acfer 094 AOAs. These results indicate AOAs originated from a single homogeneous reservoir.

SIMS minor element analyses reveal uniform FeO contents of olivine in AOAs from DOM 08006 (∼0.05 wt%), suggesting AOAs formed at more reducing environments in the solar nebula than previously thought. In contrast, EPMA-derived FeO contents of the same AOA olivine are systematically higher than those obtained by SIMS analyses, indicating that EPMA-derived FeO contents of AOA olivine tend to be influenced by fluorescence from surrounding matrix materials and/or Fe,Ni-metals in AOAs.

Magnesium isotopes of Kaba and DOM 08006 AOA olivines are negatively mass-dependently fractionated down to –3.8‰ from the chondritic value, indicative of a disequilibrium condensation origin for some AOAs. Olivine grains from compact AOAs show limited variations in δ^{25}Mg ranging from –1.2‰ to –0.2‰. In contrast, larger variations in δ^{25}Mg, ranging from –3.8‰ to –0.4‰, are observed in olivine grains from pore-rich AOAs. The latter data are positively correlated with their CrO contents, suggesting that the variation in Mg isotope ratios was related to condensation temperature during formation. In contrast, the limited variation in δ^{25}Mg of compact AOAs likely resulted from partial isotope exchange with ambient gas through high-temperature annealing.

Magnesium isotope ratios of five Wild 2 olivine particles are consistent with mass-dependent fractionation from a chondritic Mg isotopic composition, indicating that Wild 2 olivine particles formed in the chondritic reservoir with respect to Mg isotope compositions. Three ^{16}O-rich Wild 2 olivines have small variations in δ^{25}Mg, ranging from –1.0‰ to 0.6‰. Considering their minor element abundances, these particles may have experienced complex thermal histories including condensation followed by annealing. Two ^{16}O-depleted Wild 2 olivines have near-chondritic Mg isotope ratios, supporting an origin that is similar to meteoritic chondrules.

One ^{16}O-rich Wild 2 LIME olivine particle, T77/F50, shows agreement in terms of chemical and isotopic compositions with olivines in pore-rich AOAs from DOM 08006, suggesting that T77/F50 formed by disequilibrium condensation near the proto-Sun. If this is the case, this olivine particle likely traveled to the outer solar protoplanetary disk and then was accreted during the formation of comet 81P/Wild 2.

Declaration of Competing Interest

The authors declare that they have no known competing financial interests or personal relationships that could have appeared to influence the work reported in this paper.

instrumentation was provided by NSF through the University of Wisconsin Materials Research Science and Engineering Center (DMR-1720415).

APPENDIX A. SUPPLEMENTARY MATERIAL

Supplementary data to this article can be found online at https://doi.org/10.1016/j.gca.2020.09.036.

REFERENCES

Aléon J., Krot A. N. and McKeegan K. D. (2002) Calcium-aluminum-rich inclusions and amoeboid olivine aggregates from the CR carbonaceous chondrites. *Meteorit. Planet. Sci.* **37**, 1729–1755.

Ando K., Kurokawa H. and Oishi Y. (1981) Self-diffusion coefficient of oxygen in Single-crystal forsterite. *J. Am. Ceram. Soc.* **64**, C30.

Baertschi P. (1976) Absolute ^{18}O content of standard mean ocean water. *Earth Planet. Sci. Lett.* **31**, 341–344.

Bodénan J. D., Starkey N. A., Russell S. S., Wright I. P. and Franchi I. A. (2014) An oxygen isotope study of Wark-Lovering rims on type A CAIs in primitive carbonaceous chondrites. *Earth Planet. Sci. Lett.* **401**, 327–336.

Bonal L., Quirico E., Bourot-Denise M. and Montagnac G. (2006) Determination of the petrologic type of CV3 chondrites by Raman spectroscopy of included organic matter. *Geochim. Cosmochim. Acta* **70**, 1849–1863.

Bouvier A., Wadhwa M., Simon S. B. and Grossman L. (2013) Magnesium isotopic fractionation in chondrules from the Murchison and Murray CM2 carbonaceous chondrites. *Meteorit. Planet. Sci.* **48**, 339–353.

Bradley J. P. (2003) Interplanetary dust particles. In *Treatise on Geochemistry* (eds. H. Holland and K. Turekian). Elsevier, Oxford, pp. 689–711.

Bridges J. C., Changela H. G., Nayakshin S., Starkey N. A. and Franchi I. A. (2012) Chondrule fragments from Comet Wild2: Evidence for high temperature processing in the outer Solar System. *Earth Planet. Sci. Lett.* **341–344**, 186–194.

Brownlee D. E. (2014) The Stardust mission: Analyzing samples from the edge of the Solar System. *Annu. Rev. Earth Planet. Sci.* **42**, 179–205.

Brownlee D. E., Tsou P., Aléon J., Alexander C. M. O. D., Araki T., Bajt S., Baratta G. A., Bastien R., Bland P., Bleuet P., Borg J., Bradley J. P., Brearley A., Brenker F., Brennan S., Bridges J. C., Browning N. D., Brucato J. R., Bullock E., Burchell M. J., Busemann H., Butterworth A., Chaussidon M., Cheuvront A., Chi M., Cintala M. J., Cordier P., Daghlian C., Dai Z., Hendecourt L. D., Djouadi Z., Economou T. E., Fakra S., Fairey S. A. J., Fallon S., Gillet P., Gilmour J., Glavin D. P., Gounelle M., Grady M. M., Huth J., Hutcheon I. D., Ignatyev K., Ishii H., Ito M., Jurewicz A., Kearsley A. T., Keller L. P., Khodja H., Kilcoyne A. L. D., Matrajt G., Mckeegan K., Meibom A., Mennella V., Messenger K., Perkins D., Perronnet M., Pianetta P., Rao W., Rietmeijer F. J. M., Schwandt C. S., See T. H., Schlutter D., Simionovici A., Simon S., Sitnitsky I., Snead C. J., Wooden D., Wopenka B., Wozniakiewicz P. and Wright I. (2006) Comet 81P/Wild 2 under a microscope. *Science* **314**, 1711–1716.

Brownlee D. E., Joswiak D. J. and Matrajt G. (2012) Overview of the rocky component of Wild 2 comet samples: Insight into the early solar system, relationship with meteoritic materials and the differences between comets and asteroids. *Meteorit. Planet. Sci.* **470**, 453–470.

Burchell M. J., Fairey S. A. J., Wozniakiewicz P., Brownlee D. E., Hörz F., Kearsley A. T., See T. H., Tsou P., Westphal A., Green S. F., Trigo-Rodríguez J. M. and Domínguez G. (2008) Characteristics of cometary dust tracks in Stardust aerogel and laboratory calibrations. *Meteorit. Planet. Sci.* **43**, 23–40.

Buse B., Wade J., Llovet X., Kearns S. and Donovan J. J. (2018) Secondary fluorescence in WDS: The role of spectrometer positioning. *Microsc. Microanal.* **24**, 604–611.

Catanzaro E. J., Murphy T. J., Garner E. L. and Shields W. R. (1966) Absolute isotopic abundance ratios and atomic weight of magnesium. *J. Res. Natl. Bur. Stand. Sect. A Phys. Chem.* **70A**, 453–458.

Chakraborty S. (2010) Diffusion coefficients in olivine, wadsleyite and ringwoodite. *Rev. Mineral. Geochem.* **72**, 603–639.

Chaumard N., Defouilloy C., Joswiak D. J., Brownlee D. E., Westphal A. J. and Kita N. T. (2018) Oxygen three-isotope ratios of particles from the comet 81P/Wild 2: Systemtaic within individual tracks. *49th Lunar Planet Sci. Conf.* **2163**.

Chen H. W., Claydon J. L., Elliott T., Coath C. D., Lai Y. J. and Russell S. S. (2018) Chronology of formation of early solar system solids from bulk Mg isotope analyses of CV3 chondrules. *Geochim. Cosmochim. Acta* **227**, 19–37.

Chi M., Ishii H. A., Simon S. B., Bradley J. P., Dai Z., Joswiak D., Browning N. D. and Matrajt G. (2009) The origin of refractory minerals in comet 81P/Wild 2. *Geochim. Cosmochim. Acta* **73**, 7150–7161.

Ciesla F. J. (2007) Outward transport of high-temperature materials around the midplane of the solar nebula. *Science* **318**, 613–615.

Clayton R. N., Onuma N., Grossman L. and Mayeda T. K. (1977) Distribution of the pre-solar component in Allende and other carbonaceous chondrites. *Earth Planet. Sci. Lett.* **34**, 209–224.

Clayton R. N., Mayeda T. K., Goswami J. N. and Olsen E. J. (1991) Oxygen isotope studies of ordinary chondrites. *Geochim. Cosmochim. Acta* **55**, 2317–2337.

Coogan L. A., Hain A., Stahl S. and Chakraborty S. (2005) Experimental determination of the diffusion coefficient for calcium in olivine between 900°C and 1500°C. *Geochim. Cosmochim. Acta* **69**, 3683–3694.

Davidson J., Alexander C. M. O., Stroud R. M., Busemann H. and Nittler L. R. (2019) Mineralogy and petrology of Dominion Range 08006: A very primitive CO3 carbonaceous chondrite. *Geochim. Cosmochim. Acta* **265**, 259–278.

Davis A. M., Richter F. M., Mendybaev R. A., Janney P. E., Wadhwa M. and McKeegan K. D. (2015) Isotopic mass fractionation laws for magnesium and their effects on26Al–26Mg systematics in solar system materials. *Geochim. Cosmochim. Acta* **158**, 245–261.

Defouilloy C., Nakashima D., Joswiak D. J., Brownlee D. E., Tenner T. J. and Kita N. T. (2017) Origin of crystalline silicates from Comet 81P/Wild 2: Combined study on their oxygen isotopes and mineral chemistry. *Earth Planet. Sci. Lett.* **465**, 145–154.

Desch S. J., Kalyaan A. and Alexander C. M. O. (2018) The effect of Jupiter's formation on the distribution of refractory elements and inclusions in meteorites. *Astrophys. J. Suppl. Ser.* **238**, 11.

Ebel D. S., Weisberg M. K. and Beckett J. R. (2012) Thermochemical stability of low-iron, manganese-enriched olivine in astrophysical environments. *Meteorit. Planet. Sci.* **47**, 585–593.

Fagan T. J., Krot A. N., Keil K. and Yurimoto H. (2004) Oxygen isotopic evolution of amoeboid olivine aggregates in the reduced CV3 chondrites Efremovka, Vigarano, and Leoville. *Geochim. Cosmochim. Acta* **68**, 2591–2611.

Fournelle J. H., Kim S. and Perepezko J. H. (2005) Monte Carlo simulation of Nb Kα secondary fluorescence in EPMA:

Comparison of PENELOPE simulations with experimental results. *Surf. Interface Anal.* **37**, 1012–1016.

Frank D. R., Zolensky M. E. and Le L. (2014) Olivine in terminal particles of Stardust aerogel tracks and analogous grains in chondrite matrix. *Geochim. Cosmochim. Acta* **142**, 240–259.

Fujiya W., Hoppe P., Ushikubo T., Fukuda K., Lindgren P., Lee M. R., Koike M., Shirai K. and Sano Y. (2019) Migration of D-type asteroids from the outer Solar System inferred from carbonate in meteorites. *Nat. Astron.* **3**, 910–915.

Fukuda K., Joswiak D. J., Brownlee D. E., Beard B. L., Spicuzza M. J., Tenner T. J., Kimura M. and Kita N. T. (2019a) The relationship between oxygen and magnesium isotope ratios in olivine from the comet 81P/Wild 2: A comparison with AOAs in primitive meteorites.. *50th Lunar Planet. Sci. Conf.* **1989**.

Fukuda K., Hiyagon H., Fujiya W., Takahata N., Kagoshima T. and Sano Y. (2019b) Origin of the short-lived radionuclide ^{10}Be and its implications for the astronomical setting of CAI formation in the solar protoplanetary disk. *Astrophys. J.* **886**, 11 pp.

Fukuda K., Beard B. L., Dunlap D. R., Spicuzza M. J., Fournelle J. H., Wadhwa M. and Kita N. T. (2020) Magnesium isotope analysis of olivine and pyroxene by SIMS: Evaluation of matrix effects. *Chem. Geol.* **540**, 119482.

Gainsforth Z., Butterworth A. L., Stodolna J., Westphal A. J., Huss G. R., Nagashima K., Ogliore R., Brownlee D. E., Joswiak D., Tyliszczak T. and Simionovici A. S. (2015) Constraints on the formation environment of two chondrule-like igneous particles from comet 81P/Wild 2. *Meteorit. Planet. Sci.* **50**, 976–1004.

Galy A., Yoffe O., Janney P. E., Williams R. W., Cloquet C., Alard O., Halicz L., Wadhwa M., Hutcheon I. D., Ramon E. and Carignan J. (2003) Magnesium isotope heterogeneity of the isotopic standard SRM980 and new reference materials for magnesium-isotope-ratio measurements. *J. Anal. At. Spectrom.* **18**, 1352.

Grossman L. and Steele I. M. (1976) Amoeboid olivine aggregates in the Allende meteorite. *Geochim. Cosmochim. Acta* **40**, 149–155.

Han J. and Brearley A. J. (2015) Microstructural evidence for complex formation histories of amoeboid olivine aggregates from the ALHA77307 CO3.0 chondrite. *Meteorit. Planet. Sci.* **50**, 904–925.

Hertwig A. T., Kimura M., Ushikubo T., Defouilloy C. and Kita N. T. (2019) The ^{26}Al-^{26}Mg systematics of FeO-rich chondrules from Acfer 094: Two chondrule generations distinct in age and oxygen isotope ratios. *Geochim. Cosmochim. Acta* **253**, 111–126.

Hölz F., Ron B., Borg J., Bradley J. P., Bridges J. C., Brownlee D. E., Burchell M. J., Chi M., Cintala M. J., Dai Z. R., Djouadi Z., Dominguez G., Economou T. E., Fairey S. A. J., Floss C., Franchi I. A., Graham G. A., Green S. F., Heck P., Hoppe P., Huth J., Ishii H., Kearsley A. T., Kissel J., Leitner J., Leroux H., Marhas K., Messenger K., Schwandt C. S., See T. H., Snead C., Stadermann F. J., Stephan T., Stroud R., Teslich N., Trigo-Rodríguez J. M., Tuzzolino A. J., Troadec D., Tsou P., Warren J., Westphal A., Wozniakiewicz P., Wright I. and Zinner E. (2006) Impact features on Stardust: Implications for Comet 81P/Wild 2 dust. *Science* **314**, 1716–1719.

Hughes A. L. H. and Armitage P. J. (2010) Particle transport in evolving protoplanetary disks: Implications for results from Stardust. *Astrophys. J.* **719**, 1633–1653.

Ishii H., Stadermann F. J., Floss C., Joswiak D. J., Bradley J. P., Teslich N., Brownlee D. E., Matrajt G., Macpherson G. J. and McKeegan K. D. (2010) Lack of evidence for in situ decay of Aluminum-26 in comet 81P/Wild 2 CAI-like refractory particles "Inti" and "Coki". *40th Lunar Planet Sci. Conf.* **2317**.

Itoh S., Russell S. S. and Yurimoto H. (2007) Oxygen and magnesium isotopic compositions of amoeboid olivine aggregates from the Semarkona LL3.0 chondrite. *Meteorit. Planet. Sci.* **42**, 1241–1247.

Jacobsen B., Yin Q.-Z., Moynier F., Amelin Y., Krot A. N., Nagashima K., Hutcheon I. D. and Palme H. (2008) ^{26}Al-^{26}Mg and ^{207}Pb-^{206}Pb systematics of Allende CAIs: Canonical solar initial ^{26}Al/^{27}Al ratio reinstated. *Earth Planet. Sci. Lett.* **272**, 353–364.

Jollands M. C., Hermann J., St. O'Neill H. C., Spandler C. and Padrón-Navarta J. A. (2016) Diffusion of Ti and some divalent cations in olivine as a function of temperature, oxygen fugacity, chemical potentials and crystal orientation. *J. Petrol.* **57**, 1983–2010.

Jollands M. C., O'Neill H. S. C., Van Orman J., Berry A. J., Hermann J., Newville M. and Lanzirotti A. (2018) Substitution and diffusion of Cr^{2+} and Cr^{3+} in synthetic forsterite and natural olivine at 1200–1500 °C and 1 bar. *Geochim. Cosmochim. Acta* **220**, 407–428.

Joswiak D. J., Brownlee D. E., Matrajt G., Westphal A. J., Snead C. J. and Gainsforth Z. (2012) Comprehensive examination of large mineral and rock fragments in Stardust tracks: Mineralogy, analogous extraterrestrial materials, and source regions. *Meteorit. Planet. Sci.* **47**, 471–524.

Joswiak D. J., Nakashima D., Brownlee D. E., Matrajt G., Ushikubo T., Kita N. T., Messenger S. and Ito M. (2014) Terminal particle from Stardust track 130: Probable Al-rich chondrule fragment from comet Wild 2. *Geochim. Cosmochim. Acta* **144**, 277–298.

Joswiak D. J., Brownlee D. E., Nguyen A. N. and Messenger S. (2017) Refractory materials in comet samples. *Meteorit. Planet. Sci.* **52**, 1612–1648.

Kita N. T., Nagahara H., Tachibana S., Tomomura S., Spicuzza M. J., Fournelle J. H. and Valley J. W. (2010) High precision SIMS oxygen three isotope study of chondrules in LL3 chondrites: Role of ambient gas during chondrule formation. *Geochim. Cosmochim. Acta* **74**, 6610–6635.

Kita N. T., Ushikubo T., Knight K. B., Mendybaev R. A., Davis A. M., Richter F. M. and Fournelle J. H. (2012) Internal ^{26}Al-^{26}Mg isotope systematics of a Type B CAI: Remelting of refractory precursor solids. *Geochim. Cosmochim. Acta* **86**, 37–51.

Klöck W., Thomas K. L., McKay D. S. and Palme H. (1989) Unusual olivine and pyroxene composition in interplanetary dust and unequilibrated ordinary chondrites. *Nature* **339**, 126–128.

Komatsu M., Krot A. N., Petaev M. I., Ulyanov A. A., Keil K. and Miyamoto M. (2001) Mineralogy and petrography of amoeboid olivine aggregates from the reduced CV3 chondrites Efremovka, Leoville and Vigarano: Products of nebular condensation, accretion and annealing. *Meteorit. Planet. Sci.* **36**, 629–641.

Komatsu M., Mikouchi T. and Miyamoto M. (2009) High-temperature annealing of amoeboid olivine aggregates: Heating experiments on olivine-anorthite mixtures. *Polar Sci.* **3**, 31–55.

Komatsu M., Fagan T. J., Mikouchi T., Petaev M. I. and Zolensky M. E. (2015) LIME silicates in amoeboid olivine aggregates in carbonaceous chondrites: Indicator of nebular and asteroidal processes. *Meteorit. Planet. Sci.* **50**, 1271–1294.

Komatsu M., Fagan T. J., Krot A. N., Nagashima K., Petaev M. I., Kimura M. and Yamaguchi A. (2018) First evidence for silica condensation within the solar protoplanetary disk. *Proc. Natl. Acad. Sci.* **115**, 7497–7502.

Kööp L., Nakashima D., Heck P. R., Kita N. T., Tenner T. J., Krot A. N., Nagashima K., Park C. and Davis A. M. (2016) New constraints on the relationship between ^{26}Al and oxygen,

calcium, and titanium isotopic variation in the early Solar System from a multielement isotopic study of spinel-hibonite inclusions. *Geochim. Cosmochim. Acta* **184**, 151–172.

Krot A. N., Petaev M. I., Russell S. S., Itoh S., Fagan T. J., Yurimoto H., Chizmadia L., Weisberg M. K., Komatsu M., Ulyanov A. A. and Keil K. (2004a) Amoeboid olivine aggregates and related objects in carbonaceous chondrites: Records of nebular and asteroid processes. *Chemie der Erde* **64**, 185–239.

Krot A. N., Petaev M. I. and Yurimoto H. (2004b) Amoeboid olivine aggregates with low-Ca pyroxenes: A genetic link between refractory inclusions and chondrules? *Geochim. Cosmochim. Acta* **68**, 1923–1941.

Krot A. N., Park C. and Nagashima K. (2014) Amoeboid olivine aggregates from CH carbonaceous chondrites. *Geochim. Cosmochim. Acta* **139**, 131–153.

Larimer J. W. (1967) Chemical fractionations in meteorites-I. Condensation of the elements. *Geochim. Cosmochim. Acta* **31**, 1215–1238.

Larsen K. K., Trinquier A., Paton C., Schiller M., Wielandt D., Ivanova M. A., Connelly J. N., Nordlund Å., Krot A. N. and Bizzarro M. (2011) Evidence for magnesium isotope heterogeneity in the solar protoplanetary disk. *Astrophys. J. Lett.* **735**, 7 pp.

Larsen K. K., Wielandt D., Schiller M., Krot A. N. and Bizzarro M. (2020) Episodic formation of refractory inclusions in the Solar System and their presolar heritage. *Earth Planet. Sci. Lett.* **535**, 116088.

Leitner J., Hoppe P. and Heck P. R. (2010) Fisrt discovery of presolar material of possible supernova origin in impact residues from comet 81P/Wild 2. *41th Lunar Planet. Sci. Conf.* **1607**.

Leitner J., Heck P. R., Hoppe P. and Huth J. (2012) The C-, N- and O-isotopic composition of cometary dust from comet 81P/Wild 2. *43rd Lunar Planet. Sci. Conf.* **1839**.

Liu M. C., McKeegan K. D., Goswami J. N., Marhas K. K., Sahijpal S., Ireland T. R. and Davis A. M. (2009) Isotopic records in CM hibonites: Implications for timescales of mixing of isotope reservoirs in the solar nebula. *Geochim. Cosmochim. Acta* **73**, 5051–5079.

Lodders K. (2003) Solar system abundances and condensation temperatures of the elements. *Astrophys. J.* **591**, 1220–1247.

Ludwig K. R. (2012) *User's Manual for Isoplot 3.75.* Berkley Geochronology Center, Special Publication, pp. 1–75.

MacPherson G. J., Kita N. T., Ushikubo T., Bullock E. S. and Davis A. M. (2012) Well-resolved variations in the formation ages for Ca-Al-rich inclusions in the early Solar System. *Earth Planet. Sci. Lett.* **331–332**, 43–54.

MacPherson G. J., Bullock E. S., Tenner T. J., Nakashima D., Kita N. T., Ivanova M. A., Krot A. N., Petaev M. I. and Jacobsen S. B. (2017) High precision Al–Mg systematics of forsterite-bearing Type B CAIs from CV3 chondrites. *Geochim. Cosmochim. Acta* **201**, 65–82.

Makide K., Nagashima K., Krot A. N., Huss G. R., Hutcheon I. D. and Bischoff A. (2009) Oxygen- and magnesium-isotope compositions of calcium-aluminum-rich inclusions from CR2 carbonaceous chondrites. *Geochim. Cosmochim. Acta* **73**, 5018–5050.

Marrocchi Y., Villeneuve J., Jacquet E., Piralla M. and Chaussidon M. (2019a) Rapid condensation of the first Solar System solids. *Proc. Natl. Acad. Sci.* **116**, 23461–23466.

Marrocchi Y., Euverte R., Villeneuve J., Batanova V., Welsch B., Ferrière L. and Jacquet E. (2019b) Formation of CV chondrules by recycling of amoeboid olivine aggregate-like precursors. *Geochim. Cosmochim. Acta* **247**, 121–141.

Matrajt G., Ito M., Wirick S., Messenger S., Brownlee D. E. and Joswiak D. (2008) Carbon investigation of two Stardust particles: A TEM, NanoSIMS, and XANES study. *Meteorit. Planet. Sci.* **43**, 315–334.

Matzel J. E. P., Ishii H. A., Joswiak D. J., Hutcheon I. D., Bradley J. P., Brownlee D. E., Weber P. K., Teslich N., Matrajt G., McKeegan K. D. and MacPherson G. J. (2010) Constraints on the formation age of cometary material from the NASA Stardust mission. *Science* **328**, 483–486.

McKeegan K. D., Aléon J., Bradley J., Brownlee D. E., Busemann H., Butterworth A., Chaussidon M., Fallon S., Floss C., Gilmour J., Gounelle M., Graham G., Guan Y., Heck P. R., Hoppe P., Hutcheon I. D., Huth J., Ishii H., Ito M., Jacobsen S. B., Kearsley A., Leshin L. A., Liu M. C., Lyon I., Marhas K. K., Marty B., Matrajt G., Meibom A., Messenger S., Mostefaoui S., Mukhopadhyay S., Nakamura-Messenger K., Nittler L., Palma R., Pepin R. O., Papanastassiou D. A., Robert F., Schlutter D., Snead C. J., Stadermann F. J., Stroud R., Tsou P., Westphal A., Young E. D., Ziegler K., Zimmermann L. and Zinner E. (2006) Isotopic compositions of cometary matter returned by stardust. *Science* **314**, 1724–1728.

McKeegan K. D., Kallio A. P. A., Heber V. S., Jarzebinski G., Mao P. H., Coath C. D., Kunihiro T., Wiens R. C., Nordholt J. E., Moses R. W., Reisenfeld D. B., Jurewicz A. J. G. and Burnett D. S. (2011) The oxygen isotopic composition of the sun inferred from captured solar wind. *Science* **332**, 1528–1532.

Messenger S., Joswiak D. J., Ito M., Matrajt G. and Brownlee D. E. (2009) Discovery of presolar SiC from comet WILD-2. *40th Lunar Planet. Sci. Conf.* **1790**.

Morioka M. (1981) Cation diffusion in olivine-II. Ni-Mg, Mn-Mg, Mg and Ca. *Geochim. Cosmochim. Acta* **45**, 1573–1580.

Nagashima K., Krot A. N. and Huss G. R. (2015) Oxygen-isotope compositions of chondrule phenocrysts and matrix grains in Kakangari K-grouplet chondrite: Implication to a chondrule-matrix genetic relationship. *Geochim. Cosmochim. Acta* **151**, 49–67.

Nakamura-Messenger K., Keller L. P., Clemett S. J., Messenger S. and Ito M. (2011) Nanometer-scale anatomy of entire Stardust tracks. *Meteorit. Planet. Sci.* **46**, 1033–1051.

Nakamura T., Noguchi T., Tsuchiyama A., Ushikubo T., Kita N. T., Valley J. W., Zolensky M. E., Kakazu Y., Sakamoto K., Mashio E., Uesugi K. and Nakano T. (2008) Chondrulelike objects in short-period Comet 81P/Wild 2. *Science* **321**, 1664–1667.

Nakashima D., Ushikubo T., Joswiak D. J., Brownlee D. E., Matrajt G., Weisberg M. K., Zolensky M. E. and Kita N. T. (2012) Oxygen isotopes in crystalline silicates of comet Wild 2: A comparison of oxygen isotope systematics between Wild 2 particles and chondritic materials. *Earth Planet. Sci. Lett.* **357–358**, 355–365.

Nakashima D., Ushikubo T., Kita N. T., Weisberg M. K., Zolensky M. E. and Ebel D. S. (2015) Late formation of a comet Wild 2 crystalline silicate particle, Pyxie, inferred from Al-Mg chronology of plagioclase. *Earth Planet. Sci. Lett.* **410**, 54–61.

Neveu M. and Vernazza P. (2019) IDP-like asteroids formed later than 5 Myr after Ca–Al-rich inclusions. *Astrophys. J.* **875**, 30.

Ogliore R. C., Huss G. R., Nagashima K., Butterworth A. L., Gainsforth Z., Stodolna J., Westphal A. J., Joswiak D. and Tyliszczak T. (2012) Incorporation of a late-forming chondrule into comet Wild 2. *Astrophys. J. Lett.* **745**, 1–5.

Ogliore R. C., Nagashima K., Huss G. R., Westphal A. J., Gainsforth Z. and Butterworth A. L. (2015) Oxygen isotopic composition of coarse- and fine-grained material from comet 81P/Wild 2. *Geochim. Cosmochim. Acta* **166**, 74–91.

Olsen M. B., Krot A. N., Larsen K., Paton C., Wielandt D., Schiller M. and Bizzarro M. (2011) Whole-rock ^{26}Al-^{26}Mg systematics of amoeboid olivine aggregates from the oxidized

CV3 carbonaceous chondrite Allende. *Meteorit. Planet. Sci.* **46**, 1688–1702.

Olsen M. B., Wielandt D., Schiller M., Van Kooten E. M. M. E. and Bizzarro M. (2016) Magnesium and [54]Cr isotope compositions of carbonaceous chondrite chondrules – Insights into early disk processes. *Geochim. Cosmochim. Acta* **191**, 118–138.

Park C., Nagashima K., Krot A. N., Huss G. R., Davis A. M. and Bizzarro M. (2017) Calcium-aluminum-rich inclusions with fractionation and unidentified nuclear effects (FUN CAIs): II. Heterogeneities of magnesium isotopes and [26]Al in the early Solar System inferred from in situ high-precision magnesium-isotope measurements. *Geochim. Cosmochim. Acta* **201**, 6–24.

Petaev M. I. and Wood J. A. (2005) Meteoritic constraints on temperatures, pressures, cooling rates, chemical compositions, and modes of condensation in the solar nebula. In *Chondrites and the Protoplanetary Disk, ASP Conference Series* (eds. A. N. Krot, E. R. D. Scott and B. Reipurth). Astronomical Society of the Pacific, San Francisco, California, pp. 373–406.

Pettke T., Oberli F., Audétat A., Wiechert U., Harris C. R. and Heinrich C. A. (2011) Quantification of transient signals in multiple collector inductively coupled plasma mass spectrometry: Accurate lead isotope ratio determination by laser ablation of individual fluid inclusions. *J. Anal. At. Spectrom.* **26**, 475–492.

Richter F. M. (2004) Timescales determining the degree of kinetic isotope fractionation by evaporation and condensation. *Geochim. Cosmochim. Acta* **68**, 4971–4992.

Rubin A. E. (2013) An amoeboid olivine inclusion (AOI) in CK3 NWA 1559, comparison to AOIs in CV3 Allende, and the origin of AOIs in CK and CV chondrites. *Meteorit. Planet. Sci.* **48**, 432–444.

Ruzicka A., Floss C. and Hutson M. (2012) Amoeboid olivine aggregates (AOAs) in the Efremovka, Leoville and Vigarano (CV3) chondrites: A record of condensate evolution in the solar nebula. *Geochim. Cosmochim. Acta* **79**, 79–105.

Sandford S. A. (2008) Terrestrial analysis of the organic component of comet dust. *Annu. Rev. Anal. Chem.*, 549–578.

Sandford S. A., Aleon J., Alexander C. M. O., Araki T., Bajt S., Baratta G. A., Borg J., Bradley J. P., Brownlee D. E., Brucato J. R., Burchell M. J., Busemann H., Butterworth A., Clemett S. J., Cody G., Colangeli L., Cooper G., Hendecourt L. D., Djouadi Z., Dworkin J. P., Ferrini G., Fleckenstein H., Flynn G. J., Franchi I. A., Fries M., Gilles M. K., Glavin D. P., Gounelle M., Grossemy F., Jacobsen C., Keller L. P., Kilcoyne A. L. D., Leitner J., Matrajt G., Meibom A., Mennella V., Mostefaoui S., Nittler L. R., Palumbo M. E., Papanastassiou D. A., Robert F., Rotundi A., Snead C. J., Spencer M. K., Stadermann F. J., Steele A., Stephan T., Tsou P., Tyliszczak T., Westphal A. J., Wirick S., Wopenka B., Yabuta H., Zare R. N. and Zolensky M. E. (2006) Organics captured from comet 81P/Wild 2 by the Stardust spacecraft. *Science* **314**, 1720–1724.

Simon S. B., Joswiak D. J., Ishii H. A., Bradley J. P., Chi M., Grossman L., Aléon J., Brownlee D. E., Fallon S., Hutcheon I. D., Matrajt G. and Mckeegan K. D. (2008) A refractory inclusion returned by Stardust from comet 81P/Wild 2. *Meteorit. Planet. Sci.* **43**, 1861–1877.

Simon S. B., Krot A. N. and Nagashima K. (2019) Oxygen and Al-Mg isotopic compositions of grossite-bearing refractory inclusions from CO3 chondrites. *Meteorit. Planet. Sci.* **54**, 1362–1378.

Sugiura N. and Krot A. N. (2007) [26]Al-[26]Mg systematics of Ca-Al-rich inclusions, amoeboid olivine aggregates, and chondrules from the ungrouped carbonaceous chondrite Acfer 094. *Meteorit. Planet. Sci.* **42**, 1183–1195.

Sugiura N., Petaev M. I., Kimura M., Miyazaki A. and Hiyagon H. (2009) Nebular history of amoeboid olivine aggregates. *Meteorit. Planet. Sci.* **44**, 559–572.

Teng F. Z., Li W. Y., Ke S., Marty B., Dauphas N., Huang S., Wu F. Y. and Pourmand A. (2010) Magnesium isotopic composition of the Earth and chondrites. *Geochim. Cosmochim. Acta* **74**, 4150–4166.

Tenner T. J., Nakashima D., Ushikubo T., Kita N. T. and Weisberg M. K. (2015) Oxygen isotope ratios of FeO-poor chondrules in CR3 chondrites: Influence of dust enrichment and H₂O during chondrule formation. *Geochim. Cosmochim. Acta* **148**, 228–250.

Tenner T. J., Ushikubo T., Nakashima D., Schrader D. L., Weisberg M. K., Kimura M. and Kita N. T. (2018a) Oxygen isotope characteristics of chondrules from recent studies by secondary ion mass spectrometry. In *Chondrules* (eds. S. S. Russell, H. C. Connolly and A. N. Krot). Cambridge University Press, pp. 196–246.

Tenner T. J., Kimura M. and Kita N. T. (2018b) Further characterizing the extent of metamorphism within the Dominion Range 08006 CO3 chondrite. *49th Lunar Planet. Sci. Conf.* **1510**.

Ushikubo T., Kimura M., Kita N. T. and Valley J. W. (2012) Primordial oxygen isotope reservoirs of the solar nebula recorded in chondrules in Acfer 094 carbonaceous chondrite. *Geochim. Cosmochim. Acta* **90**, 242–264.

Ushikubo T., Nakashima D., Kimura M., Tenner T. J. and Kita N. T. (2013) Contemporaneous formation of chondrules in distinct oxygen isotope reservoirs. *Geochim. Cosmochim. Acta* **109**, 280–295.

Ushikubo T., Tenner T. J., Hiyagon H. and Kita N. T. (2017) A long duration of the ^{16}O-rich reservoir in the solar nebula, as recorded in fine-grained refractory inclusions from the least metamorphosed carbonaceous chondrites. *Geochim. Cosmochim. Acta* **201**, 103–122.

Van Kooten E. M. M. E., Wielandt D., Schiller M., Nagashima K., Thomen A., Larsen K. K., Olsen M. B., Nordlund Å., Krot A. N. and Bizzarro M. (2016) Isotopic evidence for primordial molecular cloud material in metal-rich carbonaceous chondrites. *Proc. Natl. Acad. Sci.* **113**, 2011–2016.

Wai C. M. and Wasson J. T. (1977) Nebular condensation of moderately volatile elements and their abundances in ordinary chondrites. *Earth Planet. Sci. Lett.* **36**, 1–13.

Wasserburg G. J., Wimpenny J. and Yin Q.-Z. (2012) Mg isotopic heterogeneity, Al-Mg isochrons, and canonical [26]Al/[27]Al in the early solar system. *Meteorit. Planet. Sci.* **47**, 1980–1997.

Wasson J. T., Gregory K. W. and Rubin A. E. (1994) Equilibration temperatures of EL chondrites: A major downward revision in the ferrosilite contents of enstatite. *Meteoritics* **29**, 658–662.

Weisberg M. K., Prinz M., Clayton R. N. and Mayeda T. K. (1993) The CR (Renazzo-type) carbonaceous chondrite group and its implications. *Geochim. Cosmochim. Acta* **57**, 1567–1586.

Weisberg M. K., Connolly H. C. and Ebel D. S. (2004) Petrology and origin of amoeboid olivine aggregates in CR chondrites. *Meteorit. Planet. Sci.* **39**, 1741–1753.

Yang L. and Ciesla F. J. (2012) The effects of disk building on the distributions of refractory materials in the solar nebula. *Meteorit. Planet. Sci.* **47**, 99–119.

Young E. D. and Galy A. (2004) The isotope geochemistry and cosmochemistry of magnesium. *Rev. Mineral. Geochem.* **55**, 197–230.

Young E. D. and Russell S. S. (1998) Oxygen reservoirs in the early solar nebula inferred from an Allende CAI. *Science* **282**, 452–455.

Yurimoto H., Krot A. N., Choi B.-G., Aléon J., Kunihiro T. and Brearley A. J. (2008) Oxygen isotopes of chondritic components. *Rev. Mineral. Geochem.* **68**, 141–186.

Zhang M., Bonato E., King A. J., Russell S. S., Tang G. and Lin Y. (2020) Petrology and oxygen isotopic compositions of calcium-aluminum-rich inclusions in primitive CO3.0-3.1 chondrites. *Meteorit. Planet. Sci.* **55**, 911–935.

Zolensky M. E., Zega T. J., Yano H., Wirick S., Westphal A. J., Weisberg M. K., Weber I., Warren J. L., Velbel M. A., Tsuchiyama A., Tsou P., Toppani A., Tomioka N., Tomeoka K., Teslich N., Taheri M., Susini J., Stroud R., Stephan T., Stadermann F. J., Snead C. J., Simon S. B., Simionovici A., See T. H., Robert F., Rietmeijer F. J. M., Rao W., Perronnet M. C., Dimitri A., Papanastassiou, Okudaira Kyok, Ohsumi Kazumas, Ohnishi I., Nakamura-Messenger K., Nakamura T., Mostefaoui S., Mikouchi T., Meibom A., Matrajt G., Marcus M. A., Leroux H., Lemelle L., Le L., Lanzirotti A., Langenhorst F., Krot A. N., Keller L. P., Kearsley A. T., Joswiak D. J., Jacob D., Ishii H., Harvey R., Hagiya K., Grossman L., Grossman J. N., Graham G. A., Gounelle M., Gillet P., Genge M., Flynn G. J., Ferroir T., Fallon S., Ebel D. S., Dai Z. R., Cordier P., Clark B., Chi M., Butterworth A. L., Brownlee D. E., Bridges J. C., Brennan S., Brearley A., Bradley J. P., Bleuet P., Bland P. A. and Bastien R. (2006) Mineralogy and petrology of comet 81P/Wild 2 nucleus samples. *Science* **314**, 1735–1739.

Associate editor: Audrey Bouvier